EUMETSAT

ROM SAF

RADIO OCCULTATION METEOROLOGY

ROM SAF CDOP-3

Visiting Scientist Report 34:

Higher-order ionospheric correction of bending angles accounting for ionospheric asymmetry and evaluation of correction methods

Congliang Liu

ROM SAF Consortium
Danish Meteorological Institute (DMI)
European Centre for Medium-Range Weather Forecasts (ECMWF)
Institut d'Estudis Espacials de Catalunya (IEEC)
Met Office (UKMO)

Ref: SAF/ROM/DMI/REP/VS/34
Version: 1.1
Date: 10 December 2019

DOCUMENT AUTHOR TABLE

	Author(s)	*Function*	*Date*
Prepared by:	Congliang Liu	ROM SAF Visiting Scientist	08/04/2019
Reviewed by (Internal):	Stig Syndergaard	ROM SAF Scientist	05/06/2019
Approved by:	Sean Healy	ROM SAF Science Coordinator	06/12/2019
Approved by:	Kent B. Lauritsen	ROM SAF Project Manager	10/12/2019

DOCUMENT CHANGE RECORD

Version	*Date*	*By*	*Description*
Version 0.1	15 October 2018	Congliang Liu	First Draft
Version 0.2	30 October 2018	Congliang Liu	First draft after initial review by GK and SS
Version 0.3	11 April 2019	Congliang Liu	Draft final version reviewed by GK
Version 0.4	23 October 2019	Congliang Liu	Draft final version reviewed by SS and GK
Version 1.0	6 December 2019	Congliang Liu	Final version reviewed by SS and GK
Version 1.1	10 December 2019	Congliang Liu	Including additional editorial comments from KBL

DOCUMENT DISTRIBUTION LIST

This VS report is made available at the ROM SAF website.

VS AUTHOR AND DURATION

VS Authors

This VS study was carried out by Dr. Congliang Liu, Postdoc Scientist at Wegener Center for Climate and Global Change, University of Graz, Graz, Austria; Email: liucongliang66@126.com. Prof. Gottfried Kirchengast, Dr. Marc Schwä rz and Dr. Julia Danzer from the Wegener Center acted as advisers and made contributions to this VS activity.

VS Duration

This VS study was performed during March to August 2018 at the Wegener Center, University of Graz, Austria. In addition, follow-up investigations were carried out at the National Space Science Center of the Chinese Academy of Sciences (NSSC/CAS), Beijing, as part of the Joint Laboratory on Occultations for Atmosphere and Climate (JLOAC) of NSSC/CAS and University of Graz.

ROM SAF

The Radio Occultation Meteorology Satellite Application Facility (ROM SAF) is a decentralised processing center under EUMETSAT which is responsible for operational processing of GRAS radio occultation (RO) data from the Metop satellites and radio occultation data from other missions. The ROM SAF delivers bending angle, refractivity, temperature, pressure, humidity, and other geophysical variables in near real-time for NWP users, as well as reprocessed Climate Data Records (CDRs) and Interim Climate Data Records (ICDRs) for users requiring a higher degree of homogeneity of the RO data sets. The CDRs and ICDRs are further processed into globally gridded monthly-mean data for use in climate monitoring and climate science applications.

The ROM SAF also maintains the Radio Occultation Processing Package (ROPP) which contains software modules that aid users wishing to process, quality-control and assimilate radio occultation data from any radio occultation mission into NWP and other models.

The ROM SAF Leading Entity is the Danish Meteorological Institute (DMI), with Cooperating Entities: i) European Centre for Medium-Range Weather Forecasts (ECMWF) in Reading, United Kingdom, ii) Institut D'Estudis Espacials de Catalunya (IEEC) in Barcelona, Spain, and iii) Met Office in Exeter, United Kingdom. To get access to our products or to read more about the ROM SAF please go to: `http://www.romsaf.org`.

Intellectual Property Rights

List of Contents

Executive Summary

This document contains the results from the ROM SAF Visiting Scientist activity VS34 with the objectives to: (1) improve the ROM SAF level 3 products. (2) assess the baseline CDOP-3 approach (Kappa approach) in its most recent form [RD.1] against the new 'bi-local' correction approach, and investigate new techniques which could be applied in CDOP-4. (3) demonstrate the improvement of the higher-order corrections experimentally.

In order to realize these objectives, the VS34 activity was divided into the following tasks: (1) Implementation of the Kappa approach in the WEGC processing system (rOPS). (2) Evaluation and validation of the new RIE correction together with existing methods. (3) Summarising the results of the study and making recommendations.

Based on an implementation of the Bi-local correction approach and the Kappa correction approach in Wegener Center's new rOPS processing system, a first detailed evaluation and statistical comparison analysis has been performed between these two higher-order ionospheric correction approaches for RO bending angle profiles. Additionally, a comparison of these two advanced ionospheric correction approaches with the standard linear dual-frequency bending angle correction method and SABER data has been done. The study showed that the newly introduced Bi-local approach performs reasonable, and in many aspects similar to the more simple Kappa approach, though also important differences have been revealed.

Main overall conclusions that we can draw from the study include the following (Figure 0.1): (1) The mean bending angle RIE biases have a clear negative tendency, an aspect where Bi-local and Kappa approaches are closely consistent. (2) In the three components of the Bi-local term, the Ne2 term plays a dominant role; the geomagnetic term (BNe term) can be important regionally. (3) The total RIEs clearly increase with increasing solar activity, overall well captured both by Bi-local and Kappa approaches. (4) The low and middle latitude bending angle RIEs are larger than the high latitude ones, which is consistent with previous studies.

Following these overall conclusions, we can formulate some recommendations on what we learned more specifically from the performance of the Bi-local correction approach relative to the Kappa correction approach; in order to suggest what might be taken as next steps related to improving ionospheric correction in ROM SAF operational processing, if one considers to go beyond the Kappa approach:
(1) The Bi-local correction approach considers both the effects of the ionospheric electron density and the geomagnetic field, while the Kappa RIE correction approach only considers the effect of the ionosphere; therefore the Bi-local approach has more capacity to present the variability of the Earth space environment conditions that affect RO bending angles.
(2) Although the geomagnetic field term only slightly affects the global-mean climatological bending angle profiles, it can play a relevant role for contributing to the RIE of regional-mean climatological bending angle profiles.
(3) The Bi-local correction approach also accounts for the asymmetry of the ionospheric and geomagnetic conditions, which we find to have a moderate but non-negligible influence.
(4) Commonly, the bi-local bending angle RIE corrections are somewhat larger than those of the Kappa approach, while the mean profiles are often rather close. Overall, the bi-local approach is seen to capture the RIE component of the smart simplified setup of the Kappa approach, plus is capable of adding value as summarized in points (1) to (3) above.

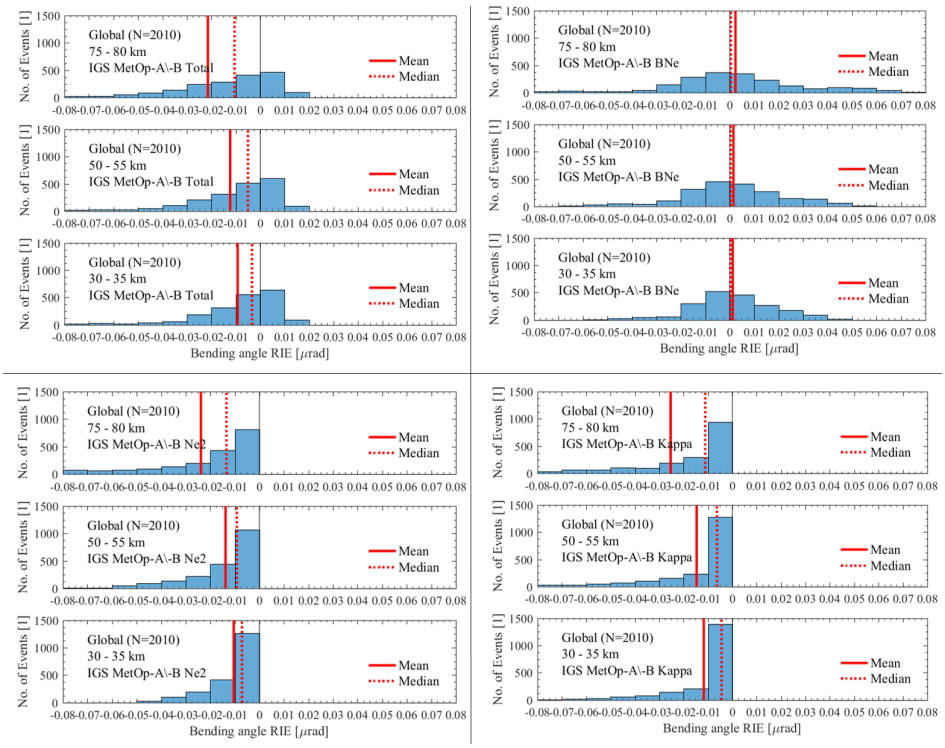

Figure 0.1: *Histogram of bending angle RIE terms in 75-80 km, 50-55 km and 30-35 km altitude ranges (vertical averages in these limited-extent layers), for the IGS case and the Metop-A/-B mission data on the two test days of 2013*

1 Introduction

1.1 Objectives and Tasks of VS34

This document contains the results from the ROM SAF Visiting Scientist activity VS34 with the objectives to:

(1) improve the ROM SAF level 3 products.

(2) assess the baseline CDOP-3 approach (Kappa approach) in its most recent form [RD.1] against the new 'bi-local' correction approach, and investigate new techniques which could be applied in CDOP-4.

(3) demonstrate the improvement of the higher-order corrections experimentally.

In order to realize these objectives, the VS34 activity was divided into the following tasks:

Task 1: Implementation of the Kappa approach in the WEGC processing system (rOPS):

A) For inter-comparison and inter-validation, implement the 'Kappa approach' correction, including the recently introduced modeling of Kappa dependences on altitude, solar zenith angle, and F10.7 [RD.1], as well as prepare the interfaces to SABER data over the stratosphere and mesosphere for the validation.

Task 2: Evaluation and validation of the new RIE correction together with existing methods:

A) Apply the new bi-local RIE correction algorithm and evaluate its performance in real retrieval system application, based on selected sets of adequately large ensembles of RO events to cover a diversity of diurnal, annual, and solar-geomagnetic activity-related variations in ionization (electron density) levels and various RO-event inbound/outbound ionospheric asymmetry patterns.

B) In the same setup, comparatively evaluate also the performance of the 'Kappa approach' correction and of the standard linear correction and finally validate all methods (bi-local correction, Kappa correction, standard correction) against ensembles of co-located profiles of the independent data from SABER over the stratosphere and mesosphere (focus region 25 km to 80 km).

Task 3: Summarising the results of the study and making recommendations:

A) Prepare a ROM SAF VS report based on the results and make recommendations for handling RIE for the ROM SAF in CDOP-3 and CDOP-4.

1.2 Background

The standard ionospheric correction of bending angles in GNSS radio occultation (RO) data removes most of the influence from the ionosphere, but leaves a residual in the data that comes from a number of sources:

(1) Small-scale ionospheric disturbances due to irregularities and turbulence as well as sharp vertical electron density gradients in the ionospheric E- and F-layers

(2) Large-scale horizontal electron density gradients in the ionosphere along the inbound and/or the outbound part of the signal paths in combination with tropospheric vertical gradients, possibly relevant in the lower troposphere

(3) Higher-order terms that are not taken into account in the standard ionospheric correction, such as due to asymmetry in electron content passed by the signals in the inbound relative to the outbound part of the propagation paths

This Visiting Scientist Activity (VSA) focuses on the third of these, having implications primarily for climate users of RO data, and described in more detail below.

The first source above can have serious implications in individual profiles, especially in those cases where the disturbances result in large scintillations in the RO signals with tangent points at stratospheric and mesospheric heights [RD.2]. Usually the most severe cases are caught in quality control, but the less severe ones, which are not caught, may degrade the quality of individual profiles to a degree that overshadows the influence from the other two sources listed above. For climate applications, where averages of large amounts of data are taken, the small-scale disturbances become less of an issue, and although it is unknown if they could collectively give rise to systematic errors on average, we do not directly address them in this study, although one should not forget their possible influence on the results.

The main influence of the second source above was only discovered recently [RD.3]. Although horizontal gradients on either the inbound or outbound parts of signal paths influence the residual in ionospheric corrected bending angles at high altitudes, the primary implications are in the lower troposphere, where the combination of the horizontal electron density gradients and large tropospheric vertical refractivity gradients may result in notable errors in the retrieved bending angle at the altitude of the vertical gradients. The mechanism is quite complicated, and although it is an interesting problem that should receive more attention in the future, the proposed work in this VSA does not explicitly address this specific aspect. However, the Task 2 work (see below), looking into various cases with variations in ionization (electron density), will include the assessment of the proposed higher-order correction at high altitudes also in cases of ionospheric horizontal gradients along the inbound/outbound paths.

The motivation for this VSA is the development of a more refined higher-order ionospheric correction scheme based on the work in [RD.4]. The idea to this refinement originated at the Wegener Center for Climate and Global Change, University of Graz (WEGC), and involves the derivation of higher-order terms taking into account the following:

(1) The higher-order influence of the ray path splitting (the term equivalent to the term also given in [RD.5] and on which the simplified approach referred to as the 'Kappa approach' [RD.6; RD.7] is based)

(2) The influence of the geomagnetic field in the series expansion of the ionospheric refractive index (addressed also in [RD.8; RD.9])

(3) The influence of the electron density at the LEO satellite

(4) The influence of horizontal gradients across the ionosphere, i.e., asymmetries in electron content between inbound (from GNSS) and outbound (towards LEO) parts

We also note the following IROWG recommendation in the Climate Sub-group [RD.10]: 'Issues of ionospheric correction and high altitude initialization should be further investigated to optimize the climate utility in the entire stratosphere. We acknowledge progress in the iono-atmo coordination workshop in 2014 and a dedicated session during the IROWG-5 workshop 2016. These efforts should continue.'

The influence of horizontal gradients across the ionosphere is difficult to handle analytically in a general way. The idea followed by the new scheme, on which the derivations are based, is therefore to assume that the horizontal electron density gradients are confined to a limited transition region between the inbound and outbound parts of the signal paths, but otherwise along each of the inbound and outbound paths the horizontal gradients are zero. In this way, the impact parameter for ray paths entering the neutral atmosphere (i.e. for rays with tangent point below the ionosphere, in practice those below 90 km altitude) is constant along the path, and the same on the inbound and outbound paths, although the electron density fields on each side are different. This is because the paths on the inbound and the outbound each experience a spherically symmetrical medium (assuming also that the neutral atmosphere is spherically symmetrical). We refer to this as 'bi-local symmetry.'

Although these assumptions are still a significant simplification, they allow the derivation of a more refined analytical expression than in previous works, which accounting with the other influences above constitutes the new correction scheme. It involves the use of an ionospheric electron density model (NeUoG/NeQuick), a geomagnetic field model (International Geomagnetic Reference Field, IGRF), and vertical total electron content (vTEC) maps (from CODE/IGS centers, deriving them from the ground-based GNSS network). The question is then how well this works under more realistic distributions of ionization than the ones assumed in the derivations, and how it compares to other existing approaches, in particular the recently introduced 'Kappa approach' [RD.5, RD.6]. A publication of the detailed derivation of the new approach of correction of higher-order residual ionospheric errors (RIEs) is currently being prepared by S. Syndergaard and G. Kirchengast [RD.11].

A key point of the proposed work will be experimental validation using RO data from Metop and other missions. Previous work on higher-order corrections has only verified the possible improvement using simulations, e.g., Refs. [RD.7; RD.8; RD.9; RD.12]. This VSA will also use simulations for verification, but will additionally attempt to demonstrate the improvement experimentally using real RO data and suitable independent validation data (from SABER). This can in principle be done by averaging a large amount of data (retrieved bending angle profiles) and then look at the change in the average at very high altitudes when the correction is applied and when it is not applied. The mean (in practice it will possibly be necessary to take the median value to exclude outliers) bending angle at high altitudes should be close to zero, or more precisely, close to the very small climatological bending angle from a model.

An experimental observation that the correction on average makes the difference even smaller, especially during day-time at solar maximum, would demonstrate the validity of the correction. Work in [RD.13] used the difference between day-time and night-time averages to correct the day-time profiles, so we know it should be possible to discern the averages under different conditions, but we do not know if any of the current correction schemes reliably removes the major part of the residual. Thus, such experimental verification will be highly valuable.

2 Methodology

2.1 Existing ionospheric correction methods

The Earth's ionosphere is a mixed neutral-and-ionized gas consisting mainly of free electrons, ions, neutral atoms and molecules, located at the altitude range of around 80 to 1000 km. Since the ionosphere is a dispersive medium, the magnitudes of GNSS signal carrier excess phases and bending angles are related to their frequency. The signal wave propagation in the ionosphere is also affected by the conditions of the geomagnetic field. For GNSS signals, the series expansion of the ionosphereic refractive index can be approximated by

$$n \approx 1 - C \cdot N_e / f^2 - K \cdot N_e B \cos\theta / f^3 - 1/2 \cdot C^2 \cdot {N_e}^2 / f^4 \tag{2.1}$$

where the two constants $C = e^2/(8\pi^2 m\varepsilon_0)$ and $K = e^3/(16\pi^3 m^2 \varepsilon_0)$, N_e is the electron density, B is the geomagnetic field strength, f is the radio wave frequency, e is the elementary charge, m is the electron mass, ε_0 is the permittivity of vacuum and θ is the angle between the magnetic field vector and the wave propagation direction. For the GPS signal frequencies ($L1$ and $L2$), $f_1 = 1.57542$ GHz and $f_2 = 1.22760$ GHz.

Nowadays, the most common approach to correcting the ionospheric effect is to use a dual-frequency linear combination of bending angles in GNSS RO data processing, as expressed by [RD.5]

$$\alpha_c(a) = (f_1^2 \alpha_1(a) - f_2^2 \alpha_2(a))/(f_1^2 - f_2^2) \tag{2.2}$$

where $\alpha_1(a)$ and $\alpha_2(a)$ are the $L1$ and $L2$ bending angles derived from the two frequency signals at the impact parameter a, and $\alpha_c(a)$ is the dual-frequency linear combination of $\alpha_1(a)$ and $\alpha_2(a)$.

Healy and Culverwell [RD.6] proposed a modification to the standard ionospheric correction of the following form

$$\alpha(a) = \alpha_1(a) + (f_2^2/(f_1^2 - f_2^2))[\alpha_1(a) - \alpha_2(a)] + \kappa(a)[\alpha_1(a) - \alpha_1(a)]^2 \tag{2.3}$$

where the term proportional to $\kappa(a)$ (hereafter referred to as κ term) compensates for the systematic residual error in the standard approach. The function, κ, can be approximated by [RD.1]

$$\kappa = A + b(f_{10.7}) + c(\chi) + e(h) \tag{2.4}$$

where A, b, c, e are coefficients, $f_{10.7}$ is the solar flux index, χ is solar zenith angle, and h is height above ground (we used impact altitude in this study).

2.2 Bi-local RIE correction approach

The bi-local correction approach was proposed and described in detail, including its theoretical derivation, by Syndergaard and Kirchengast [RD.11]. The key correction equation can be expressed by [RD.14]

$$\alpha_C(a) - \alpha(a) = -\frac{K\mathcal{F}(B_{\parallel}N_e)}{f_1 f_2 (f_1 + f_2)} - \frac{1}{2}\frac{C^2}{f_1^2 f_2^2}\frac{1}{a}\frac{\mathrm{d}[a^2\mathcal{F}(N_e^2)]}{\mathrm{d}a} - \frac{C}{(f_1^2 - f_2^2)}\frac{r_L H_L N_e(r_L)}{\sqrt{r_L^2 - a^2}}\frac{\mathrm{d}(\alpha_1 - \alpha_2)}{\mathrm{d}a}. \tag{2.5}$$

with

$$\mathcal{F}(X) = \int_a^{r_G} \left.\frac{\mathrm{d}X}{\mathrm{d}x}\right|_G \frac{a\mathrm{d}x}{\sqrt{x^2 - a^2}} + \int_a^{r_L} \left.\frac{\mathrm{d}X}{\mathrm{d}x}\right|_L \frac{a\mathrm{d}x}{\sqrt{x^2 - a^2}} - \frac{aX(r_L)}{\sqrt{r_L^2 - a^2}}, \tag{2.6}$$

where X formally denotes both the geomagnetic terms factor and the electron density-squared term factor as cntained in quation (2.5). For the input variables and the explanations of the symbols in equation 2.5 and 2.6, please refer to Table 2.3 to Table 2.6.

These are the basic equations for evaluation in this study, and the meaning of each term and their components is as defined by Syndergaard and Kirchengast [RD.14], with a bit of adjusted notation.

2.3 Solar, ionospheric and geomagnetic conditions

As shown further below, the solar, ionospheric and geomagnetic conditions are major space environment factors that affect the bending angle RIEs, therefore the ionospheric electron density and geomagnetic field intensity are main input parameters of the bi-local correction approach.

In order to investigate their effects on the bending angle RIEs, in this section the solar, ionospheric, and geomagnetic environment conditions of the chosen test days will be described via space weather indices, including F10.7 and Ap, and IGS vTEC maps. In addition, the NeUoG ionospheric electron density model and the IGRF geomagnetic field model, also used in this study, will be introduced.

2.3.1 Solar and geomagnetic activity conditions

The solar radio flux at 10.7 cm (2800 MHz) is one of the longest running records of solar activity, referred to as the F10.7 index, and can easily be measured reliably on a day-to-day basis from the Earth's surface, in all types of weather. Reported in 'solar flux units', (s.f.u.), the F10.7 can vary from below 50 s.f.u., to above 300 s.f.u., over the course of a solar cycle. Figure 2.1 shows the monthly mean time series of the F10.7 index from 2000 to 2018, and Figure 2.2 shows the time series of the daily F10.7 index for the three test months i.e., May 2013, July 2013 and July 2008, which represent high and low solar activity months [RD.15].

According to the F10.7 index, we selected the July 15th 2008 as the low solar activity test day, and May 15th 2013, July 15th 2013 as high and medium solar activity test days, in our study. The latter day is, according to the Ap index, at the same time a medium geomagnetically-perturbed day. Figure 2.1 to Figure 2.3 below illustrate these indices.

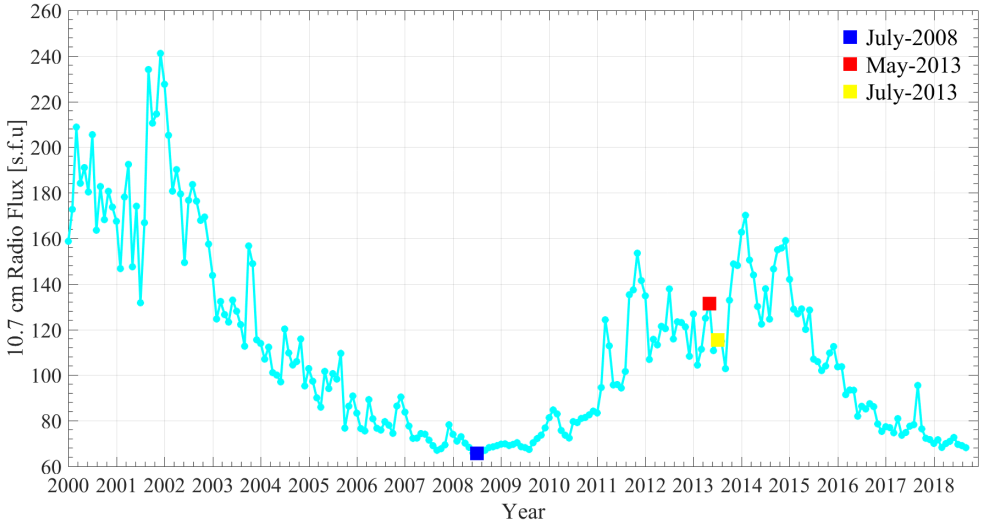

Figure 2.1: *Time series of monthly F10.7 index from 2000 to 2018*

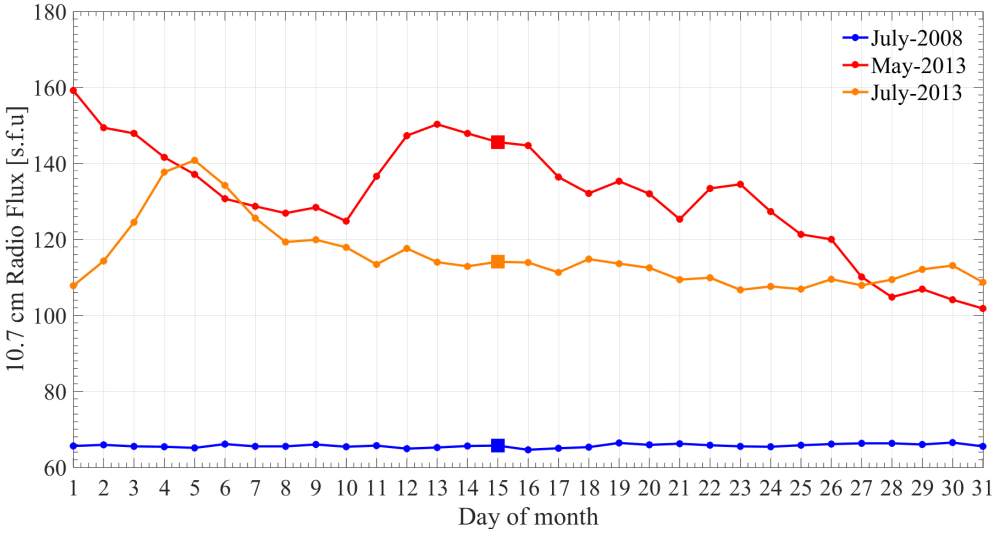

Figure 2.2: *Time series of daily F10.7 index for the three test months*

The Ap index quantifies the Earth's magnetic field intensity, which ranges from 0 to 400 and represents a Kp-value converted to a linear scale in nT (nanoTesla). Figure 2.3 shows the daily time series of the Ap index for the three test months.

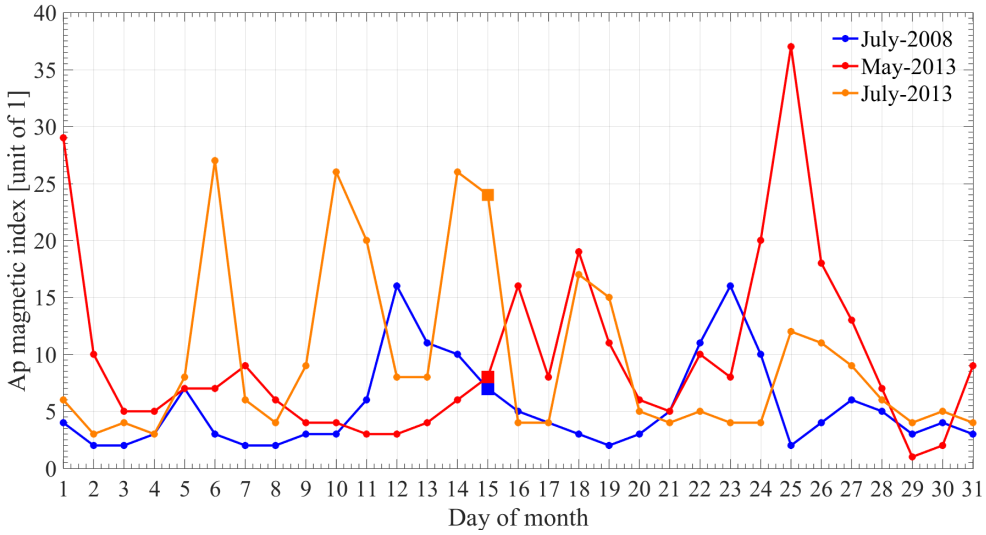

Figure 2.3: *Time series of Ap magnetic index for the three test months*

2.3.2 Ionospheric conditions and NeUoG model and vTEC maps

Regarding the ionosphere, the NeUoG (electron density university of Graz) ionospheric model was used in this study. This model represents the 3D electron density distribution as a function of local time, season, and solar activity. It well represents realistic large-scale ionospheric variability but does not include small-scale ionospheric structures.

The ionospheric electron density (Ne) profiles used in the bi-local correction approach in this study, are scaled Ne values by combining the NeUoG model electron density profiles and IGS or CODE vTEC maps. After the normalization the Ne profiles have similar curve shapes as the NeUoG model electron density and the same vTEC value as the IGS or CODE vTEC maps. Figure 2.4 shows the IGS and CODE vTEC maps for the test date July 15th 2013.

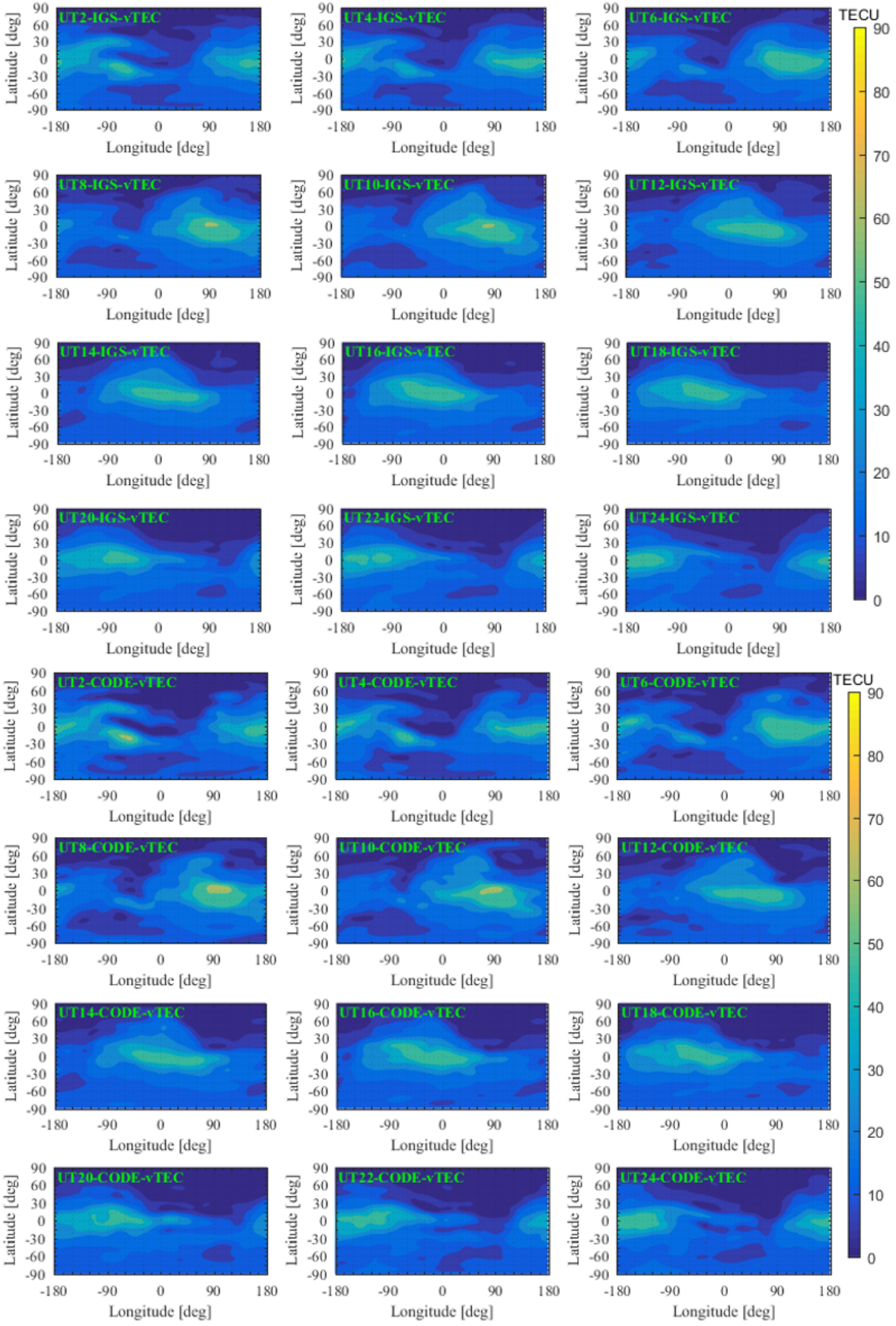

Figure 2.4: *IGS and CODE vTEC maps for July 15th 2013*

2.3.3 Geomagnetic mean field conditions and IGRF-12 model

The International Geomagnetic Reference Field (IGRF) is a series of mathematical models describing the large-scale internal part of the Earth's magnetic field between epochs 1900 A.D. and the present. It results from a collaborative effort between magnetic field modelers and institutes involved in collecting and disseminating magnetic field data from magnetic observatories, ground surveys, and low Earth orbiting (LEO) satellites. At present, each generation consists of three constituent models. One constituent is designated a Definitive Geomagnetic Reference Field (DGRF). The term 'definitive' is used because any further improvement of these retrospectively determined models is unlikely. The second constituent model, referred to as an IGRF model, is non-definitive and it will eventually be replaced by a definitive model in a future revision of the IGRF. The final constituent, referred to as the secular variation (SV), is provided to predict the time variation of the large-scale geomagnetic field for the 5 years following the latest revision of the IGRF [RD.16].

The 12th generation of the International Geomagnetic Reference Field (IGRF) was adopted in December 2014 by the Working Group V-MOD appointed by the International Association of Geomagnetism and Aeronomy (IAGA). It updates the previous IGRF generation with a definitive main field model for epoch 2010.0, a main field model for epoch 2015.0, and a linear annual predictive secular variation model for 2015.0-2020.0. Figure 2.5 shows the main geomagnetic field and its X Y Z components for the test date July 15th 2013.

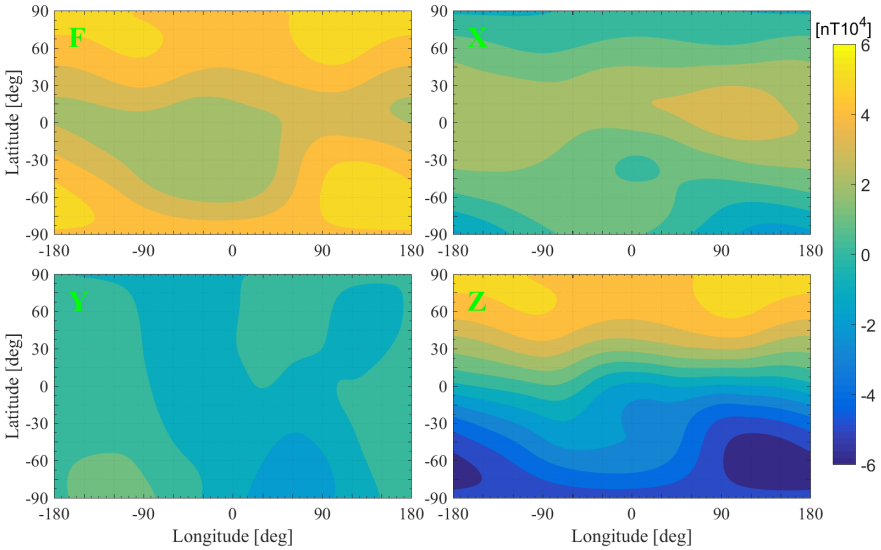

Figure 2.5: *IGRF12 model geomagnetic field maps for July 15th 2013*

2.3.4 Ionospheric and geomagnetic conditions at RO event locations

The ionospheric inbound and outbound TEC conditions as well as geomagnetic field strength conditions for the RO event locations of the test days are illustrated in this subsection. These illustrations serve to facilitate and support the understanding and interpretation of the subsequent result sections in Chapter 3.

In order to show the ionospheric and geomagnetic conditions, two scatter-plots, Figure 2.6 and Figure 2.7, show inbound vTEC (x-axis) vs. outbound vTEC (y-axis) and inbound B_{II}

(x-axis) vs. outbound B_{ll} (y-axis), respectively, of each RO event for all the data ensembles of Metop data (i.e., three test days, Metop-A and Metop-B datasets).

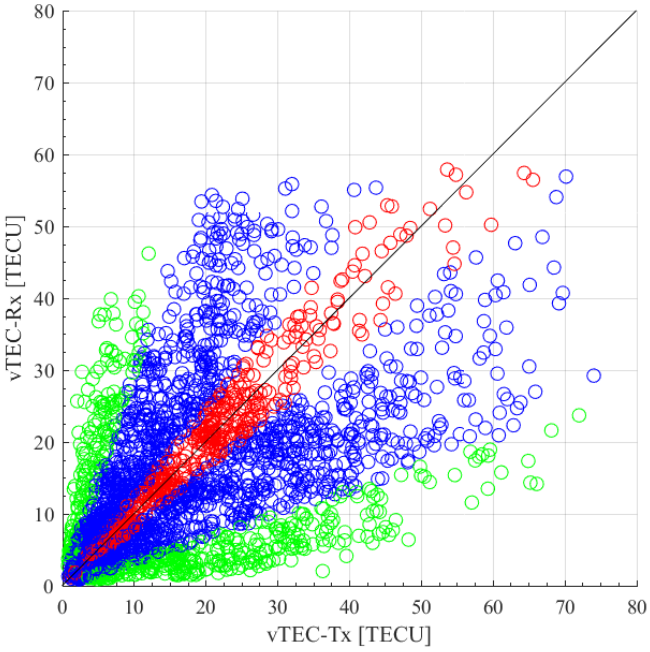

Figure 2.6: *Electron density scatter plot illustrating inbound vTEC (x-axis) vs. outbound vTEC (y-axis), classifying the ionospheric conditions into nearly symmetric (red; within +/-10% variation of inbound vs. outbound vTEC against average inbound-outbound vTEC), moderately asymmetric (blue; intermediate inbound-outbound aysmmetry), and strongly asymmetric (green; greater than +/-50% variation) RO event sub-ensembles*

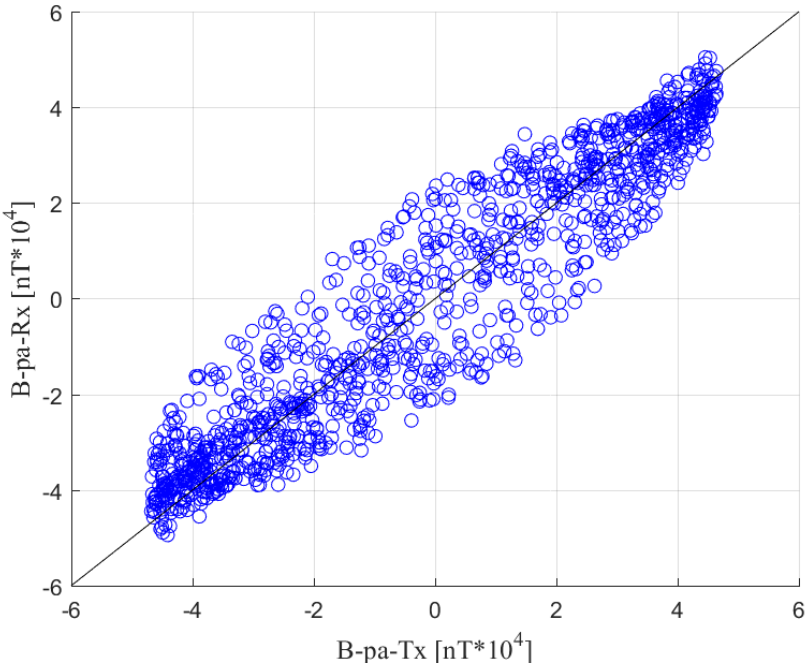

Figure 2.7: *Geomagnetic field scatter plot illustrating inbound B_{II} (x-axis) vs. outbound B_{II} (y-axis), indicating the moderate but limited asymmetries that B_{II} magnitudes typically comprise for RO event ensembles with global coverage*

2.4 Implementation of Bi-local and Kappa correction approaches in rOPS

2.4.1 Introduction of rOPS rationale and structure

Observations of the free atmosphere were historically aimed at aviation, weather research and weather forecasting, and thus the observing systems have shortcomings from a climate perspective. For climate purposes the accuracy, long-term stability, and data homogeneity were not sufficient in the respective observation records. Thus, *climate benchmark data* records, i.e., data records which are of global coverage, of high accuracy and long-term stability, which are tied to fundamental measurement standards (SI) and measure Essential Climate Variables (ECVs), are of crucial importance.

Thanks to its unique properties, the RO technique has the potential to deliver these ECV data records for thermodynamic parameters of the free atmosphere, if the uncertainties of the retrieved ECVs can be traced to the uncertainties of the RO data. This requires that the RO processing system, or *retrieval*, deriving the ECVs from the raw data, is highly accurate and that uncertainties are propagated through the processing, such that the claimed accuracy of the ECV data, expressed by the uncertainties provided, can be traced back to the raw data.

Existing retrievals at the main RO processing centers already reach high accuracy for atmospheric profiles of bending angle, refractivity, pressure, geopotential height, and temperature (< 1 K), and structural uncertainties between RO records from different processing centers are low. However, despite substantial advances in the processing of RO observations since the proof-of-concept RO mission GPS/MET in the mid 1990ties, no rigorous trace from

fundamental time (including uncertainties of side information) to the ECVs exists so far. Figure 2.8 shows a summary of how it works.

The new rOPS [RD.17], developed at the WEGC at the University of Graz, Austria, aims to realize the benchmark quality potential of RO by establishing (1) a reliably accurate retrieval with residual relative numerical uncertainties below $10^{-}4$, and (2) integrating a complete uncertainty propagation chain from the fundamental time uncertainty and relevant side influences from RO raw tracking data and high accuracy GNSS orbit data through four processors to atmospheric variables. The aim is that uncertainties can be traced from the ECVs back to the FCDR and the raw data, tied to the SI standard.

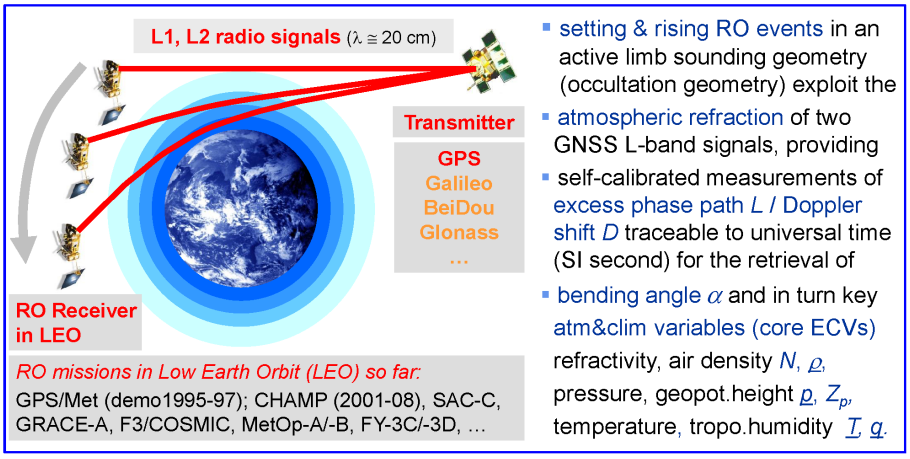

Figure 2.8: *Schematic view of the RO observing system and summary of how it works (Source: [RD.18])*

Figure 2.9 shows the main components of the rOPS as well as the main interactions, where the occultation data processing (ODP) subsystem is the core subsystem providing for the retrieval of the Level 1 and Level 2 profiles.

Overall and for input to the ODP, the two major system modeling layers, background daily system modeling and occultation event system modeling, operate once per day, and once per event, respectively. They feed the different processors of the ODP subsystem and contain several subsystems to do so. The daily system modeling (DSM) layer consists of two subsystems, the DSM geometry (DSM-Geo) and the DSM atmosphere (DSM-Atm). The event system modeling (ESM) layer consists of three subsystems, the ESM geometry and environment (ESM-GE), the ESM atmosphere (ESM-Atm) and the ESM residual bias (ESM RB).

The higher-order ionospheric corrections evaluated in this study have been integrated as prototype processing capacity, by coupling them into the ODP-L1B processor for bending angle retrieval. These integrations are introduced next below by making clear the relevant inputs and outputs of both the Kappa correction approach (subsection 2.4.2) and Bi-local correction approach (subsection 2.4.3) before we dive into results and discussions in Chapter 3.

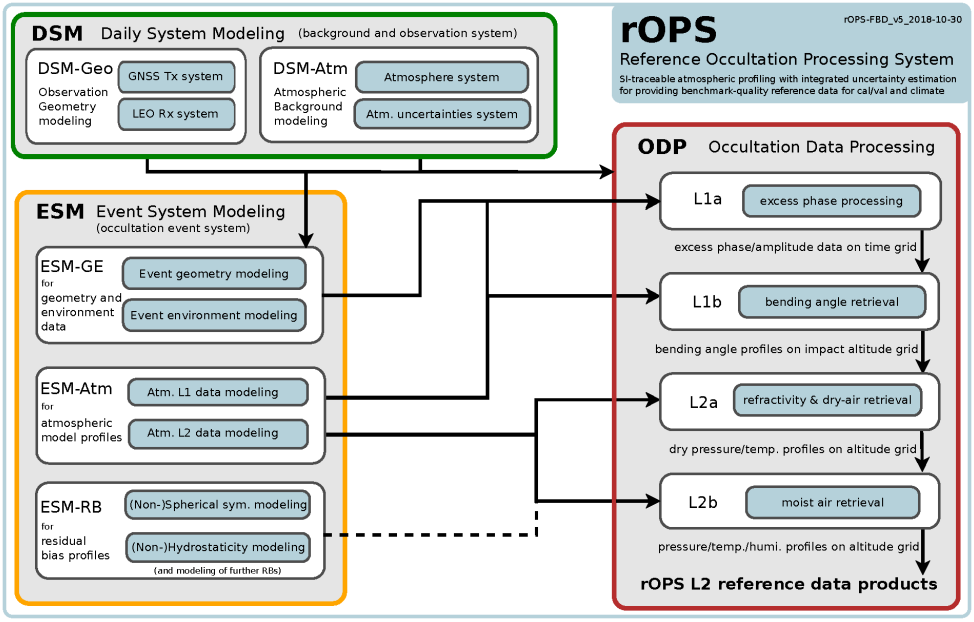

Figure 2.9: *Overview of the rOPS in form of a functional block diagram, illustrating the design and logic of the system modeling and data analysis approach, indicating its main systems and subsystems as well as its core, the occultation data processing system with the processors (Source: [RD.18])*

2.4.2 Integration of the Kappa correction approach

The Kappa approach is a comparatively simple empirical approach that was implemented following [RD.1]. Table 2.1 summarizes the limited number of input parameters and variables needed, and Table 2.2 shows the output variable profiles as function of impact altitude. Based on the outputs, on the one hand we can evaluate the Kappa coefficient that is modeled and on the other hand the complete correction where the Kappa coefficient is multiplied by the squared bending angle difference profiles between L1 and L2 frequencies (cf. the Kappa method equations in Section 2.1).

Table 2.1: *Inputs of Kappa correction approach as integrated in the rOPS*

Variable	Unit	Description
A, b, c, e		Coefficients for the empirical modeling of Kappa (cf. section 2.1)
f_k	Hz	Transmitter signal carrier frequency, with elements f_k (for GPS transmitters k = 1,2, and f_1 = 1.57542 GHz f_2 = 1.22760 GHz)
$F_{10.7}$	rad	solar flux index
χ	rad	solar zenith angle
h	m	impact altitude (profile)
α_1	rad	bending angle of L1 signal (profile)
α_2	rad	bending angle of L2 signal (profile)

Table 2.2: *Outputs of Kappa correction approach as integrated in the rOPS*

Variable	Unit	Description (both output variables are profiles as function of impact altitude)
κ	rad^{-1}	Kappa coefficient
$\triangle\alpha^{\text{Kappa}}$	rad	The Kappa residual ionospheric error (RIE)

2.4.3 Integration of the Bi-local correction approach

The Bi-local approach is a more comprehensive analytical approach that was implemented following Syndergaard and Kirchegnast [RD.14]. Tables 2.3 to 2.5 summarize the fairly comprehensive input parameters and variables needed, and Table 2.6 collects all output components of the Bi-local correction available from the rOPS for the evaluations, including the total Bi-local RIE (cf. the Bi-local method equations in Section 2.2).

Table 2.3: *(a) Basic inputs for Bi-local correction from predecessor computations in the rOPS*

Variable	Unit	Description
φ, λ, UT	*units*	Location and (reference) time of the RO event
f_k	Hz	Transmitter signal carrier frequency, with elements f_k (for GPS transmitters k = 1,2, and f_1 = 1.57542 GHz f_2 = 1.22760 GHz)
a	m	Impact parameter (profile, joint one for L1 and L2)
α_1	rad	Bending angle of L1 signal (profile)
α_2	rad	Bending angle of L2 signal (profile)
$\mathbf{r_T}$	m	Position vector of Tx satellite (ECEF: x y z)
$\mathbf{v_T}$	m/s	Velocity vector of Tx satellite (ECEF: v_x v_y v_z)
$\mathbf{r_R}$	m	Position vector of Rx satellite (ECEF: x y z)
$\mathbf{v_R}$	m/s	Velocity vector of Rx satellite (ECEF: v_x v_y v_z)
$\mathbf{x_{I350T}}$	m	Position vector of ion.mean-altitude point inbound (ECEF and Geodetic) (for the sltp60 straight-line ray, and ion.mean-altitude 350 km)
$\mathbf{x_{I350R}}$	m	Position vector of ion.mean-altitude point outbound (ECEF and Geodetic) (for the sltp60 straight-line ray, and ion.mean-altitude 350 km)

Table 2.4: *(b) Derived inputs for Bi-local correction from NeUoG ionospheric model and IGRF-12 geomagnetic model*

Variable	Unit	Description
N_e	m^{-3}	The electron density, which we calculate by using NeUoG model. The inputs for NeUoG model are as following: height (km), latitude (degree), longitude (degree), time (UT) and F10.7 index.
$vTEC^{CODE}$, $vTEC^{IGS}$	TECU ($10^{16} m^{-2}$)	vTEC map products from CODE and IGS centers.
$B_{\|\|}$, $\mathbf{B}$	nT	The geomagnetic field strength along the ray path derived from the total geomagnetic field vector $\mathbf{B}(\mathbf{X},\mathbf{Y},\mathbf{Z})$, which is obtained by using the IGRF-12 model.
$vTEC^{NeUoG}$	TECU	vTEC values from integration in NeUoG model.
$Ne(z)$	m^{-3}	$Ne(z) = (vTEC^{CODE,IGS}/vTEC^{NeUoG}) \cdot Ne^{NeUoG}(z)$, observed TEC-adjusted $Ne(z)$, either by the $vTEC$ from CODE or IGS.

Table 2.5: *(c) Input constants for Bi-local correction in the rOPS*

Variable	Unit	Description
C	$m^3 s^{-1}$	40.308 basic-ionization constant in the ion.refractivity equation
K	$m^3 T^{-1} s^{-3}$	$1.1283 \cdot 10^{12}$ magnetic-term constant in the iono.refractivity equation

Table 2.6: *Outputs of Bi-local correction approach as integrated in the rOPS*

Variable	Unit	Description (all of these RIE terms are profiles as function of impact altitude)
$\triangle\alpha^{RIE}$	rad	The total residual ionospheric error (RIE), i.e., $\alpha_c(a) - \alpha(a) = \triangle\alpha^{BNe} + \triangle\alpha^{Ne2} + \triangle\alpha^{NeL}$
$\triangle\alpha^{BNe}$	rad	The geomagnetic residual term, $\triangle\alpha^{BNe} = \triangle\alpha^{BNe}_{TxTP} + \triangle\alpha^{BNe}_{TPRx} + \triangle\alpha^{BNe}_{Rxloc}$
$\triangle\alpha^{BNe}_{TxTP}$	rad	The Tx-to-TP geomagnetic residual term
$\triangle\alpha^{BNe}_{TPRx}$	rad	The TP-to-Rx geomagnetic residual term
$\triangle\alpha^{BNe}_{Rxloc}$	rad	The Rx-local geomagnetic residual term
$\triangle\alpha^{Ne2}$	rad	The squared electron density residual term, $\triangle\alpha^{Ne2} = \triangle\alpha^{Ne2}_{TxTP} + \triangle\alpha^{Ne2}_{TPRx} + \triangle\alpha^{Ne2}_{Rxloc}$
$\triangle\alpha^{Ne2}_{TxTP}$	rad	The Tx-to-TP squared electron density residual term
$\triangle\alpha^{Ne2}_{TPRx}$	rad	The TP-to-Rx squared electron density residual term
$\triangle\alpha^{Ne2}_{Rxloc}$	rad	The Rx-local squared electron density residual term
$\triangle\alpha^{NeL}$	rad	The LEO electron density residual term

2.5 Calculation of bending angle RIE statistics

The Bi-local and Kappa correction approaches' bending angle RIEs and their component profiles were interpolated to a standard vertical grid with 550 impact altitude levels (100 m spacing between levels) in the 25-80 km range, where they will generally be illustrated in the results chapter below.

When showing statistics, the ensemble mean (bias) and ensemble standard deviations were calculated level by level for any test day(s) ensemble of individual profiles, i.e., we used the individual-profile values of the ensemble at each impact altitude level to compute these statistics measures.

3 Results and discussion

3.1 Individual RO event examples for the Bi-local RIE correction

In this section, the bending angle RIE correction performance for the Bi-local method is introduced by using individual RO event examples.

3.1.1 Ionospheric and geomagnetic conditions for RO events

In this subsection, the vertical profiles of electron density, the component of geomagnetic field, the BNe gradient and the Ne2 gradient along the raypath term are shown in Figure 3.1, Figure 3.2 and Figure 3.3 as "background illustrations" to understand the behavior of the Bi-local correction terms in accordance with the form as they are mathematically formulated in section 2.2.

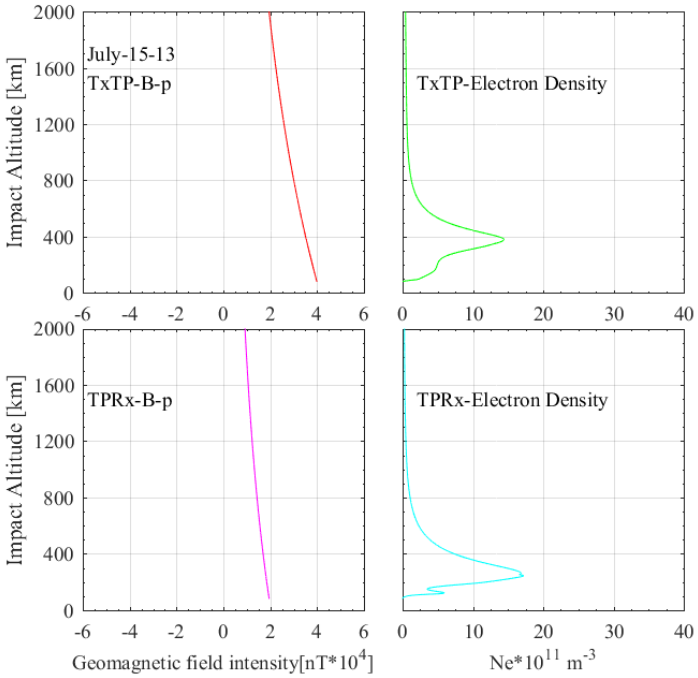

Figure 3.1: *Vertical profiles of geomagnetic field parallel to the RO raypath (B-parallel) and of electron density profiles, both at inbound (TxTP) and outbound (TPRx) raypath sides, for an example RO event*

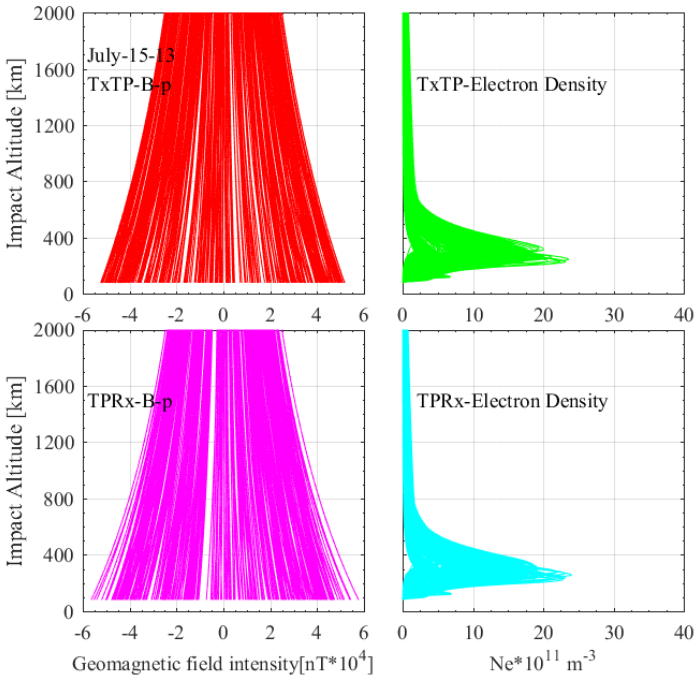

Figure 3.2: *Vertical profiles of geomagnetic field parallel to the RO raypath (B-parallel) and of electron density profiles, both at inbound (TxTP) and outbound (TPRx) raypath sides, as "bundle plot" for the ensemble dataset of July 15th 2013*

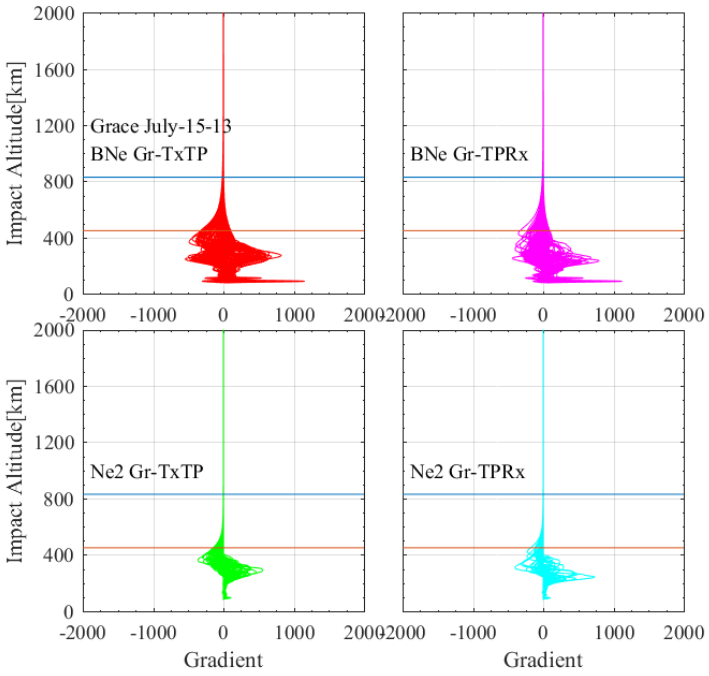

Figure 3.3: *Vertical profiles of BNe gradient and Ne2 gradient, both at inbound (TxTP) and outbound (TPRx) raypath sides, as "bundle plot" for the ensemble dataset of Grace July 15th 2013, in each subplot, the approximate LEO altitudes of Metop and GRACE satellites are marked by blue and red horizontal lines, respectively.*

3.1.2 Example individual-profile results for Bi-local RIE correction terms

In this subsection, the vertical profiles of Bi-local bending angle cerrection terms are shown by using three example RO events from the three test days, respectively, in Figure 3.4 to Figure 3.6.

To illustrate the total bi-local bending angle RIE term and its BNe, Ne2 and NeL components (cf. Table 2.6), as well as the total BNe and Ne2 terms and their inbound (Tx to tangent point) term, outbound (tangent point to Rx) term and Rx local term components, a four-panel figure structure is used.

In the 4-panel figure of the overall result (Figure 3.4), panel 1 (top left) shows the total bi-local term, while panels 2 (top right), 3 (bottom left), and 4 (bottom right) show the BNe, Ne2 and NeL components, respectively.

The order of magnitude of the NeL term is strongly related to the LEO satellite orbit altitude and the in-situ ionospheric electron density. For the Metop-A/-B missions, the order of magnitude of the NeL term is 0.001 μrad, while for the GRACE mission it is bigger, which is still very small in comparison to the Ne2 term, though. Although in this way the NeL term of GRACE mission is quite larger than that of the Metop-A/-B mission, compared with the BNe and Ne2 terms they are still very small and hence negligible in practical application.

In the 4-panel figure of the specific BNe and Ne2 term results (Figure 3.5 and Figure 3.6), panel 1 (top left) shows the total BNe or Ne2 term, while panels 2 (top right), 3 (bottom left), and 4 (bottom right) show the inbound, outbound, and Rx local components, respectively.

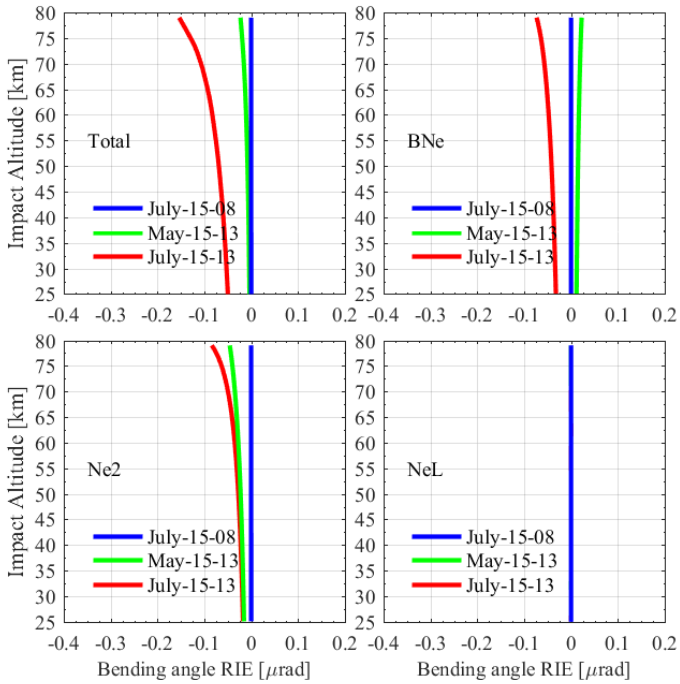

Figure 3.4: *Bi-local bending angle correction total term and its BNe, Ne2 and NeL components, for three individual example RO events from the test days*

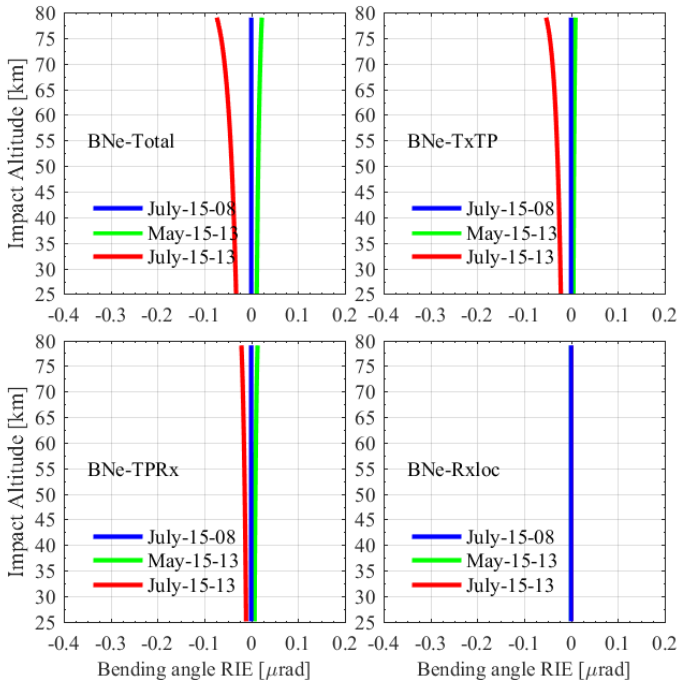

Figure 3.5: *Bi-local BNe total term and its inbound (TxTP), outbound (TPRx), and Rx location (Rxloc) components, for three individual example RO events from the test days*

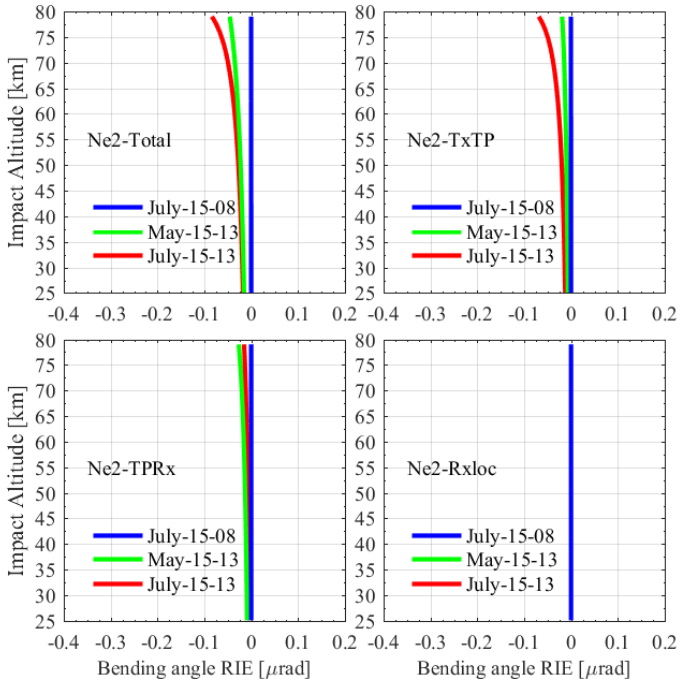

Figure 3.6: *Bi-local Ne2 total term and its inbound (TxTP), outbound (TPRx), and Rx location (Rxloc) components, for three individual example RO events from the test days*

3.2 Statistical ensemble results

In this section, the mean (bias) and standard deviation profiles of the Bi-local correction, and the Kappa correction as applicable (in subsections 3.2.4 and 3.2.5), are shown and evaluated in different geophysical and observing conditions.

The organization of the four-panel figures is analogous to Figure 3.4 to Figure 3.6 above, but here "bundle plots" of profile ensembles are shown, together with bias and standard deviation profiles, and in the results of subsection 3.2.4 the fourth panel (lower right) shows the Kappa correction result, in order to show it side-by-side with the Bi-local Ne2 correction term (lower left).

More specifically, in each panel, the light grey lines denote the individual bending angle RIE profiles, and the heavy red and green lines denote the bias and standard deviation profiles, respectively.

3.2.1 Comparison results for low and high solar activity conditions

To compare the performances of bending angle RIEs under low and high solar activity conditions, the Metop-A mission datasets on July 15th 2008 and the Metop-B mission datasets on May 15th & July 15th 2013 were used, since these neatly correspond to low and hight solar activity conditions, repectively. The results are shown in Figure 3.7 to Figure 3.15.

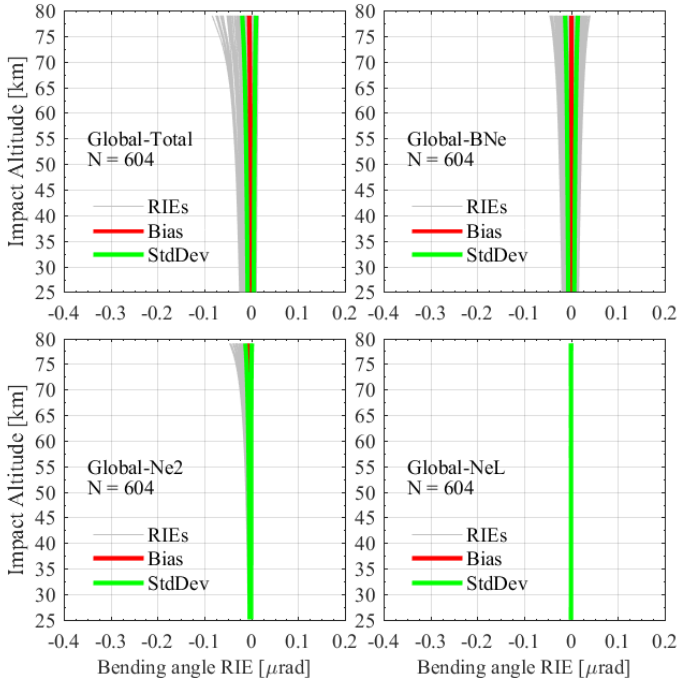

Figure 3.7: *The statistics of the bi-local total bending angle correction term and its BNe, Ne2, and NeL components, for the global ensemble dataset of the Metop-A mission RO events on July 15th 2008*

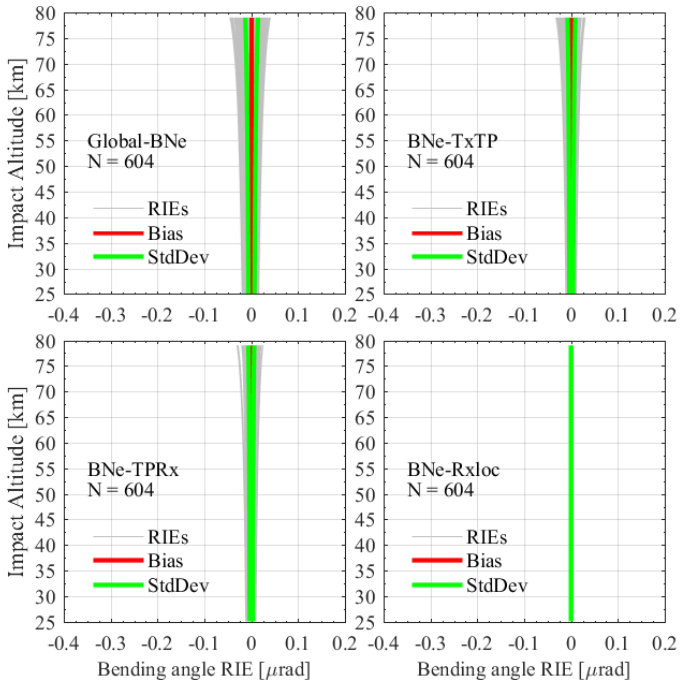

Figure 3.8: *The statistics of the bi-local BNe term and its inbound (TxTP), outbound (TPRx), and Rx location (Rxloc) components, for the global ensemble dataset of the Metop-A mission RO events on July 15th 2008*

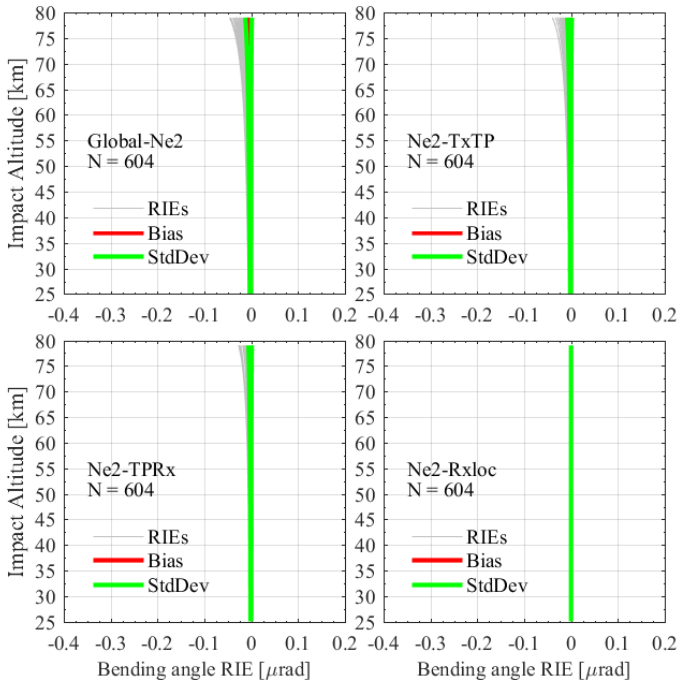

Figure 3.9: *The statistics of the bi-local Ne2 term and its inbound (TxTP), outbound (TPRx), and Rx location (Rxloc) components, for the global ensemble dataset of the Metop-A mission RO events on July 15th 2008*

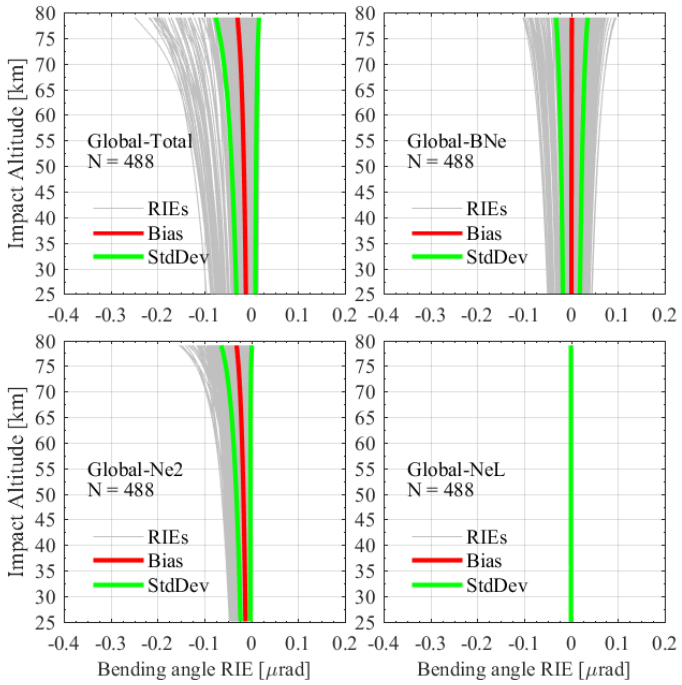

Figure 3.10: *The statistics of the bi-local total bending angle correction and its BNe, Ne2, and NeL components, for the global ensemble dataset of the Metop-B mission RO events on May 15th 2013*

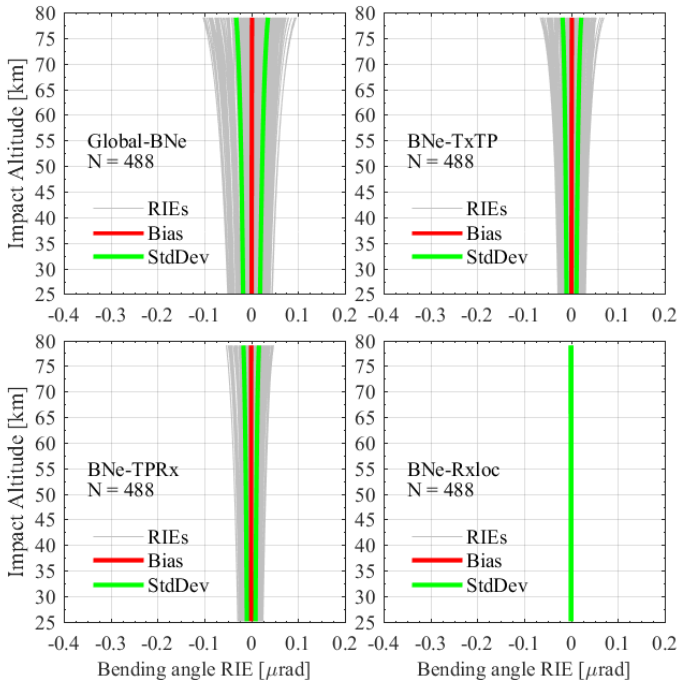

Figure 3.11: *The statistics of the bi-local BNe term and its inbound (TxTP), outbound (TPRx), and Rx location (Rxloc) components, for the global ensemble dataset of the Metop-B mission RO events on May 15th 2013*

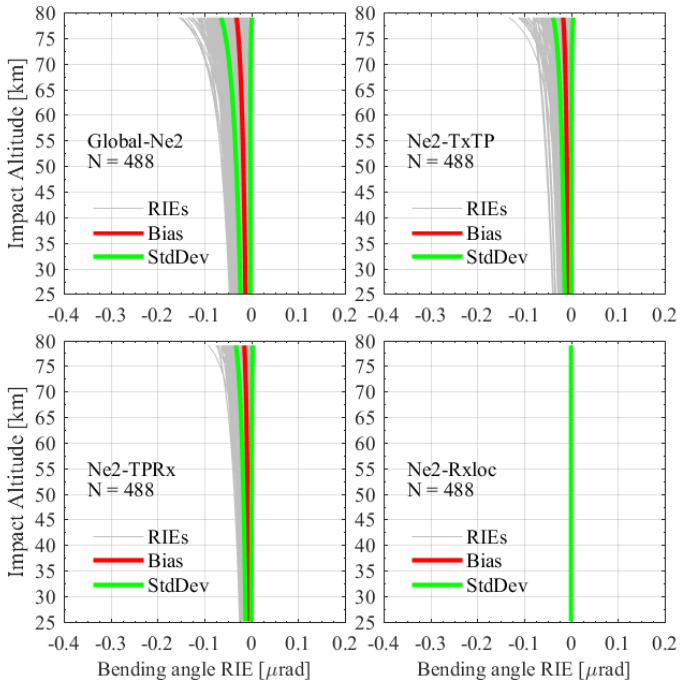

Figure 3.12: *The statistics of the bi-local Ne2 term and its inbound (TxTP), outbound (TPRx), and Rx location (Rxloc) components, for the global ensemble dataset of the Metop-B mission RO events on May 15th 2013*

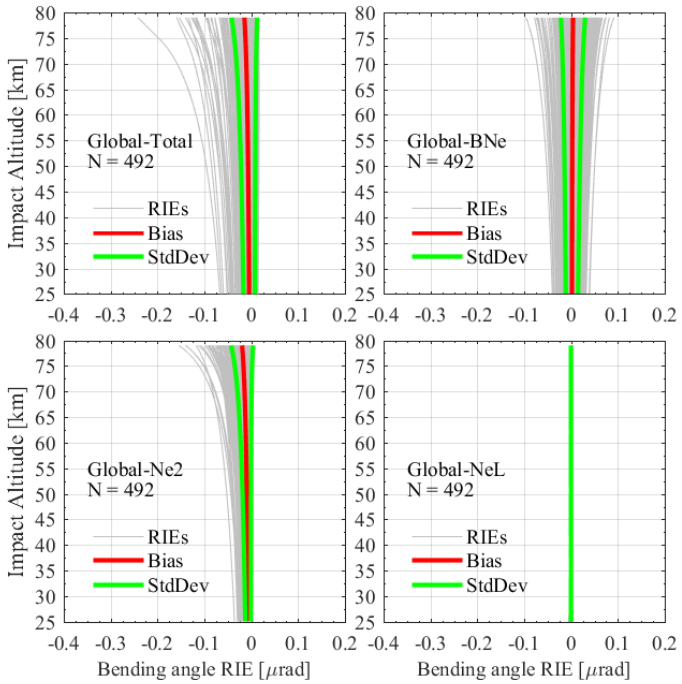

Figure 3.13: *The statistics of the bi-local total bending angle correction and its BNe, Ne2, and NeL components, for the global ensemble dataset of the Metop-B mission RO events on July 15th 2013*

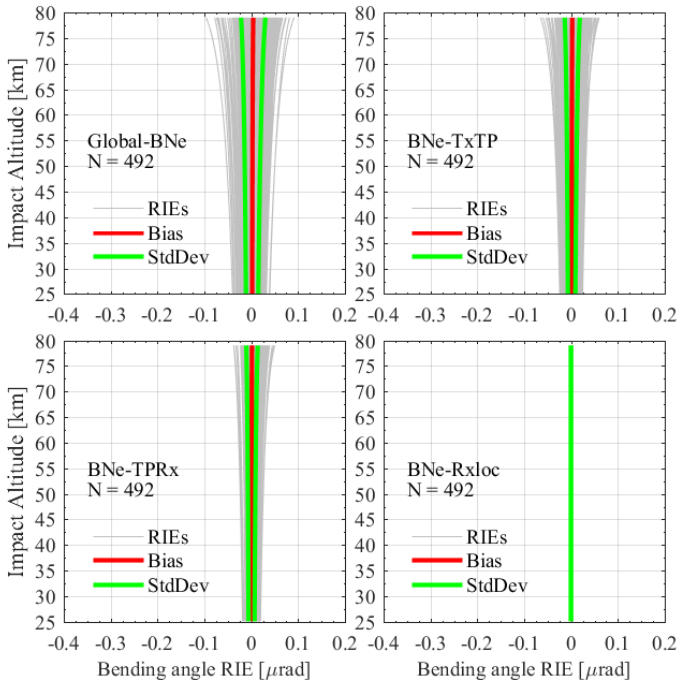

Figure 3.14: *The statistics of the bi-local BNe term and its inbound (TxTP), outbound (TPRx), and Rx location (Rxloc) components, for the global ensemble dataset of the Metop-B mission RO events on July 15th 2013*

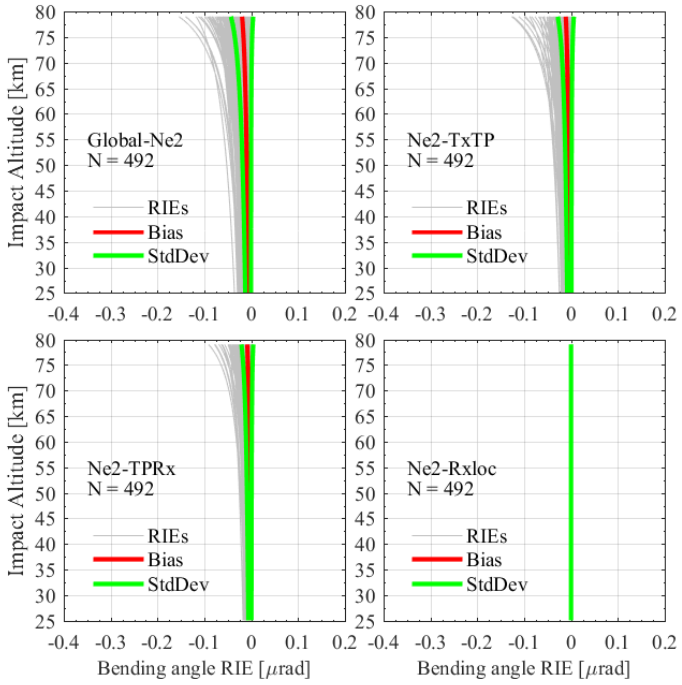

Figure 3.15: *The statistics of the bi-local Ne2 term and its inbound (TxTP), outbound (TPRx), and Rx location (Rxloc) components, for the global ensemble dataset of the Metop-B mission RO events on July 15th 2013*

From Figure 3.7 to Figure 3.15 one can see that the bending angle RIEs of the high solar

activity days are much larger than those of the low solar activity days ensemble.

Comparing the components of the BNe and Ne2 term, the BNe terms have negative and positive values, depending on the angles between the geomagnetic vector and the direction of the RO raypaths, while all the Ne2 terms are negative. The values of the Ne2 terms are systemically negative, which result in almost all the total bending angle RIE terms being negative.

Comparing the statistics of the total bending angle RIE and Ne2 term, the average bias and standard deviations are similar to each other, which means the effect of the BNe term on the global-mean climatology bending angle is very small. This is because globally the BNe terms have almost the same amounts of positive and negative profiles and cancel each other out when averaging them together. However, for regional climatology averages, the BNe term could play an important role to also leave real biases, and so may significantly affect regional-mean bias and standard deviation.

The following Figure 3.16 and Figure 3.17 show, as an example of such regional situations where the BNe term may not average out, the distribution of the RO events occurring on July 15th 2013 globally and regionally (i.e., latitude from 30S to 30N, longitude from 30E to 120E, in the regional case). As we can see from this figure tiwce as many positive BNe term RO events are located in this particular area, which may lead to non-zero BNe average.

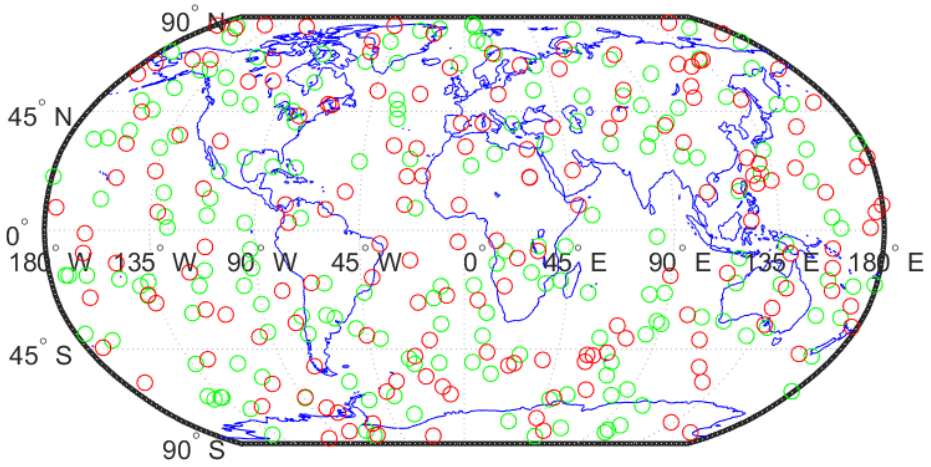

Figure 3.16: *The distribution of the Metop-B mission RO events occurring on July 15th 2013 globally*

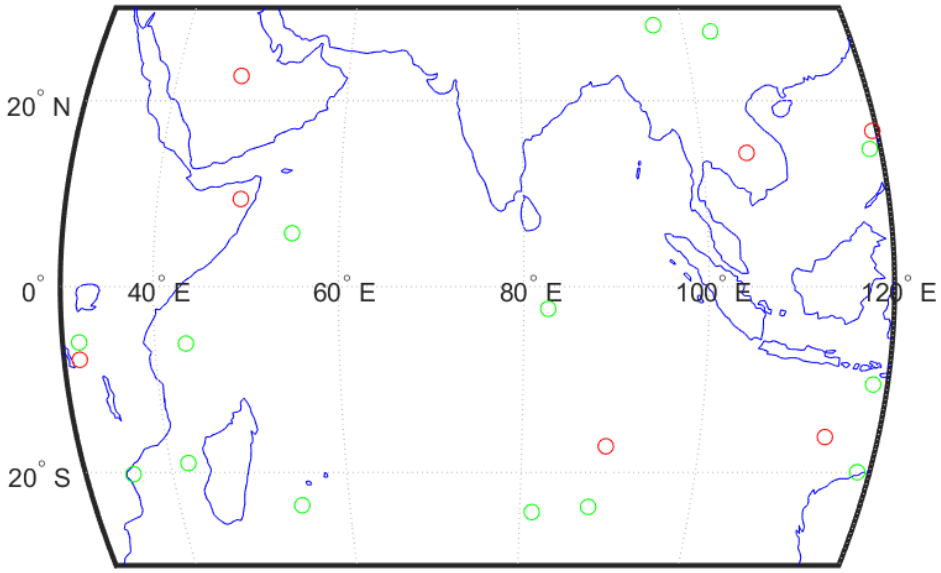

Figure 3.17: *The distribution of the Metop-B mission RO events occurring on July 15th 2013 regionally*

3.2.2 Comparison results for low and high LEO satellite orbit conditions

In this subsection, the data ensembles of GRACE and Metop-B missions data for the higher solar activity test day of July 15th 2013 were used for the comparison analysis of low and high LEO satellite orbit conditions. See Figure 3.18 to Figure 3.23 for the results.

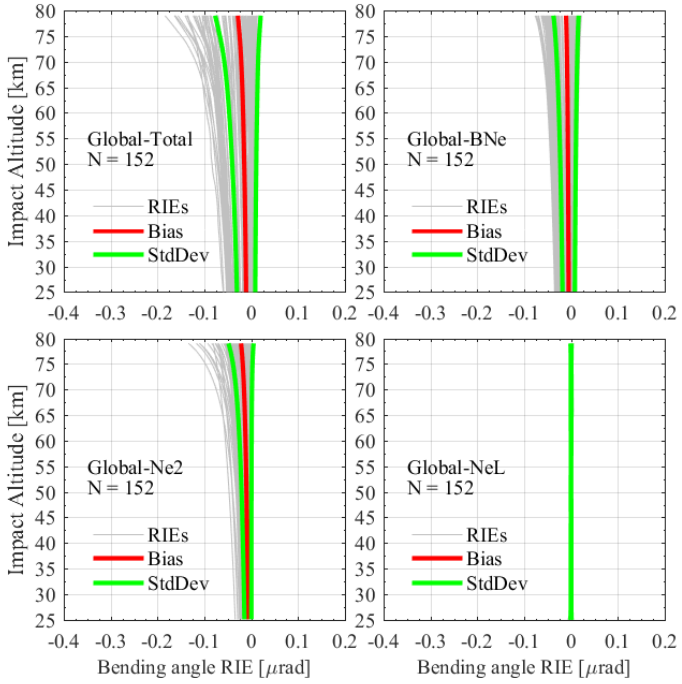

Figure 3.18: *The statistics of the bi-local total bending angle correction and its BNe, Ne2, and NeL components, for the global ensemble dataset of the GRACE mission RO events on July 15th 2013*

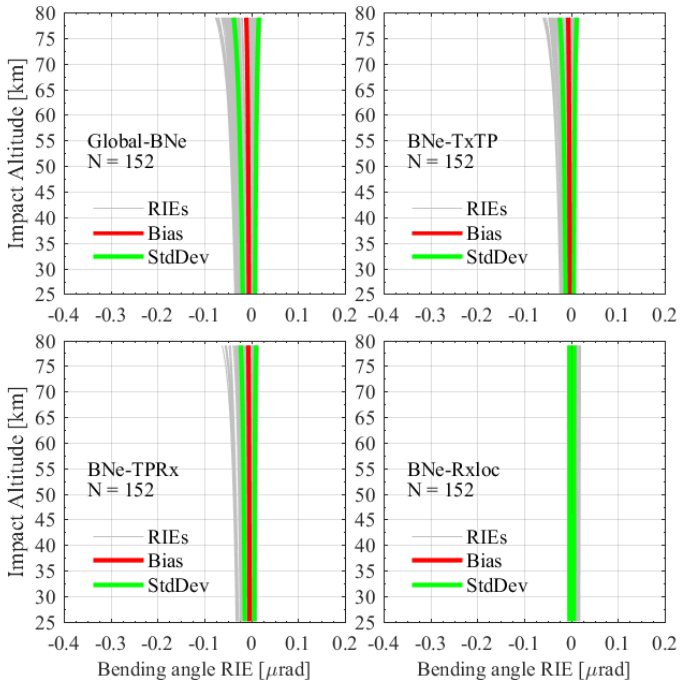

Figure 3.19: *The statistics of the bi-local BNe term and its inbound (TxTP), outbound (TPRx), and Rx location (Rxloc) components, for the global ensemble dataset of the GRACE mission RO events on July 15th 2013*

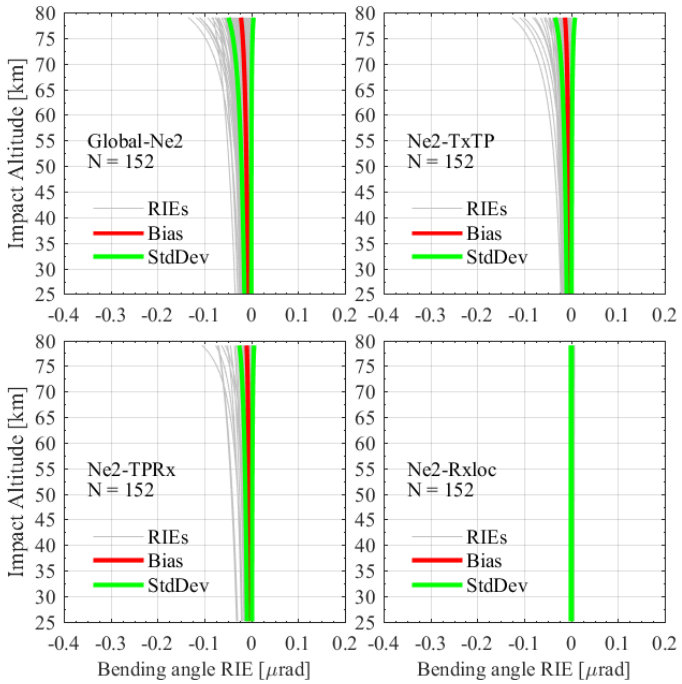

Figure 3.20: *The statistics of the bi-local Ne2 term and its inbound (TxTP), outbound (TPRx), and Rx location (Rxloc) components, for the global ensemble dataset of the GRACE mission RO events on July 15th 2013*

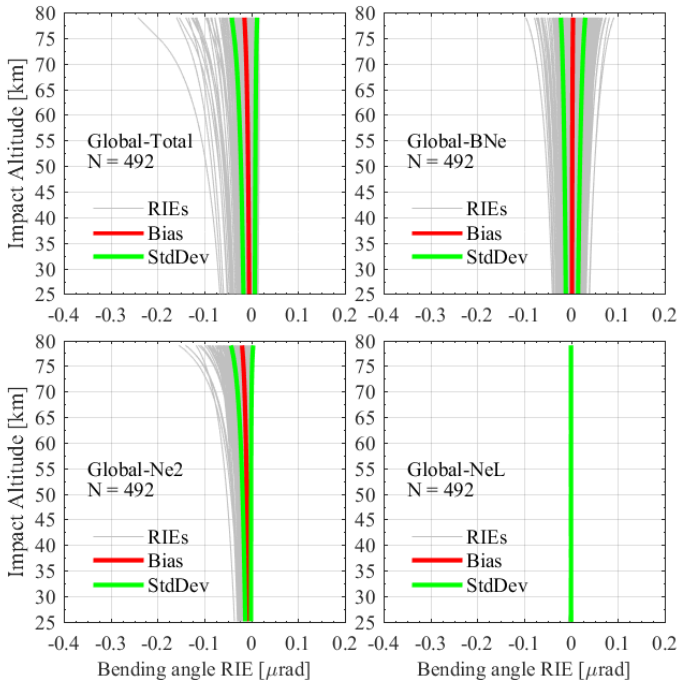

Figure 3.21: *The statistics of the bi-local total bending angle correction and its BNe, Ne2, and NeL components, for the global ensemble dataset of the Metop-B mission RO events on July 15th 2013*

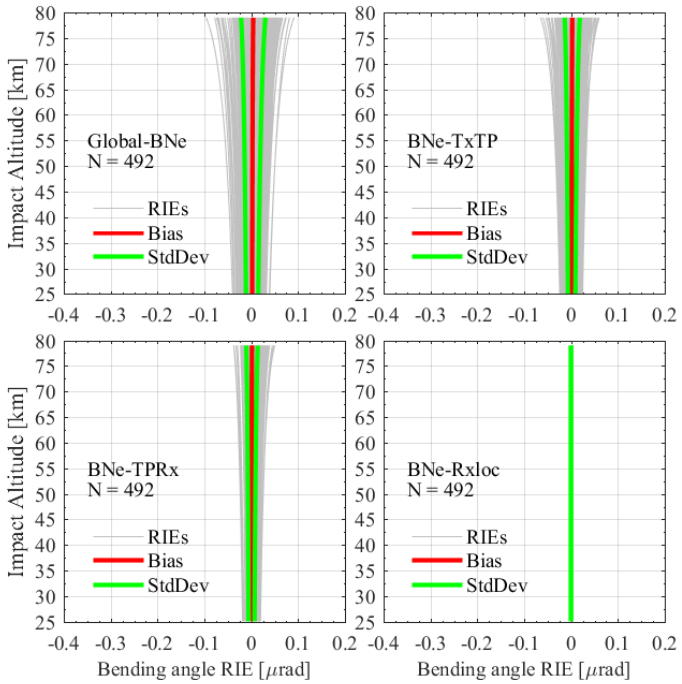

Figure 3.22: *The statistics of the bi-local BNe term and its inbound (TxTP), outbound (TPRx), and Rx location (Rxloc) components, for the global ensemble dataset of the Metop-B mission RO events on July 15th 2013*

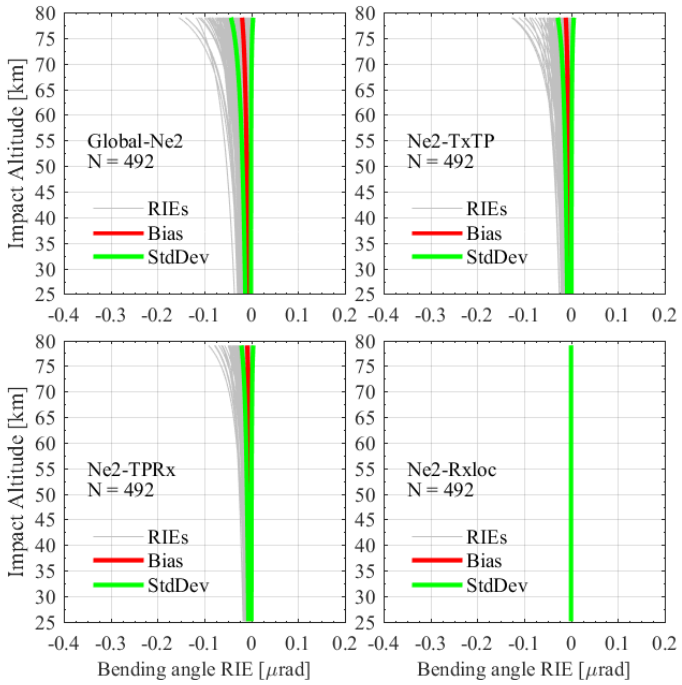

Figure 3.23: *The statistics of the bi-local Ne2 term and its inbound (TxTP), outbound (TPRx), and Rx location (Rxloc) components, for the global ensemble dataset of the Metop-B mission RO events on July 15th 2013*

As shown in the Figure 3.18 to Figure 3.23, the behaviour of GRACE data bending angle RIE profiles is similar to that of the Metop-B high-orbit-altitude satellite.

Obviously, one can see that the Rxloc LEO local term of GRACE is slightly larger than that of the Metop mission. Commonly for low LEO altitude missoins, its order of magnitude is around 0.01 μrad.

3.2.3 Comparison results for ionospheric symmetry and asymmetry conditions

According to the vTEC scatter plot in subsection 2.3.4, the RO event ensembles were divided into symmetry and asymmetry data ensembles. The dividing criterion was as follows: if the absolute value of (vTEC-Rx−vTEC-Tx)/(vTEC-Rx+vTEC-Tx) was smaller than 0.1, the corresponding RO event was classified as essentially symmetric (red dots in Figure 2.6 in section 2.3.4 above), otherwise if this value was larger than 0.5 the corresponding RO event was classified significantly asymmetric (green dots in Figure 2.6 in section 2.3.4 above).

Figure 3.24 to Figure 3.29 show the comparison of bending angle RIEs under the symmetry (SS) and asymmetry (non-spherical, NS) conditions defined in this way.

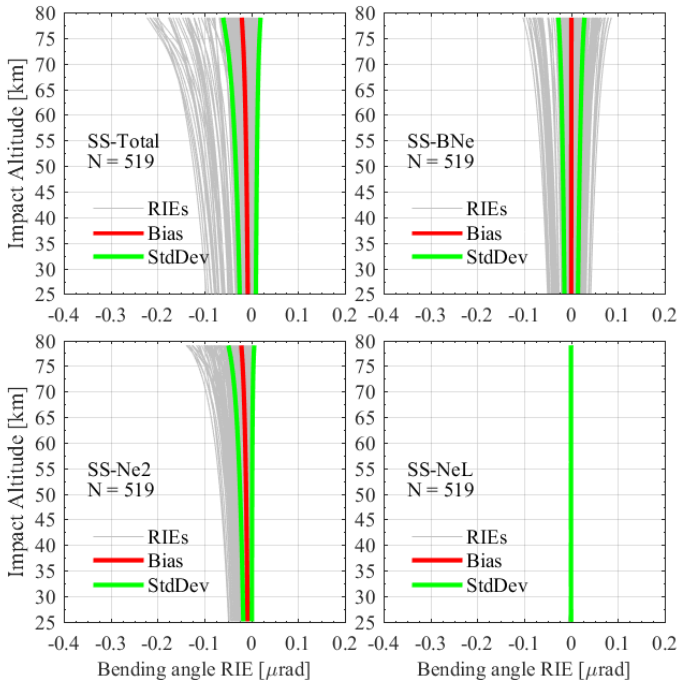

Figure 3.24: *The statistics of the total bi-local bending angle correction and its BNe, Ne2, and NeL components, for the symmetry ensemble dataset of the Metop-A/-B missions RO events occuring on the three test days*

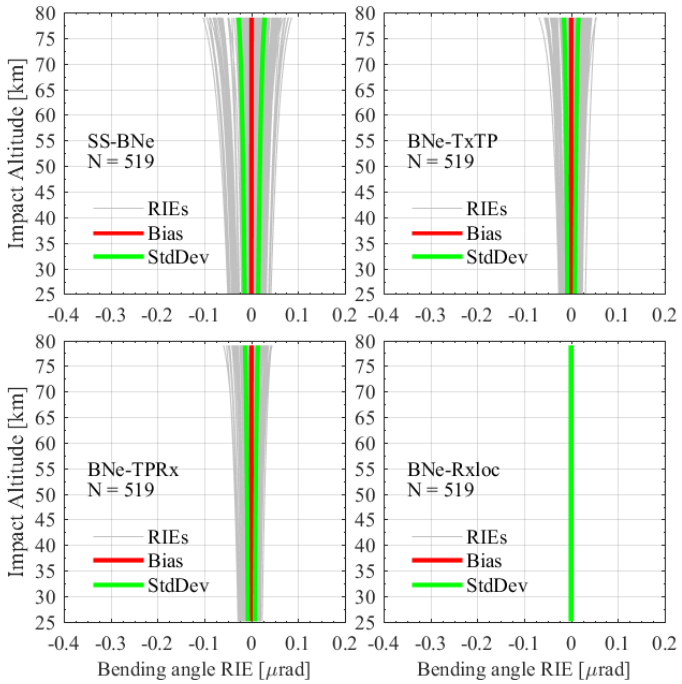

Figure 3.25: *The statistics of the bi-local BNe term and its inbound (TxTP), outbound (TPRx), and Rx location (Rxloc) components, for the symmetry ensemble dataset of the Metop-A/-B missions RO events occuring on the three test days*

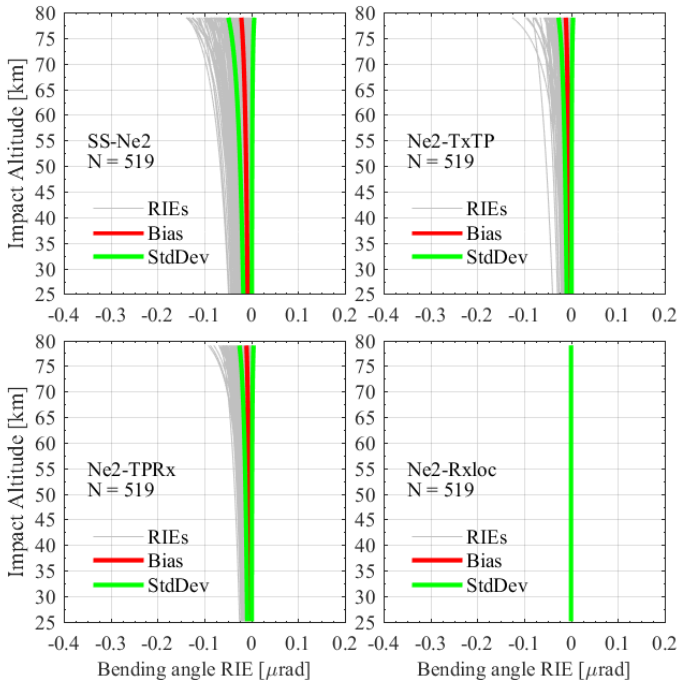

Figure 3.26: *The statistics of the bi-local Ne2 term and its inbound (TxTP), outbound (TPRx), and Rx location (Rxloc) components, for the symmetry ensemble dataset of the Metop-A/-B missions RO events occuring on the three test days*

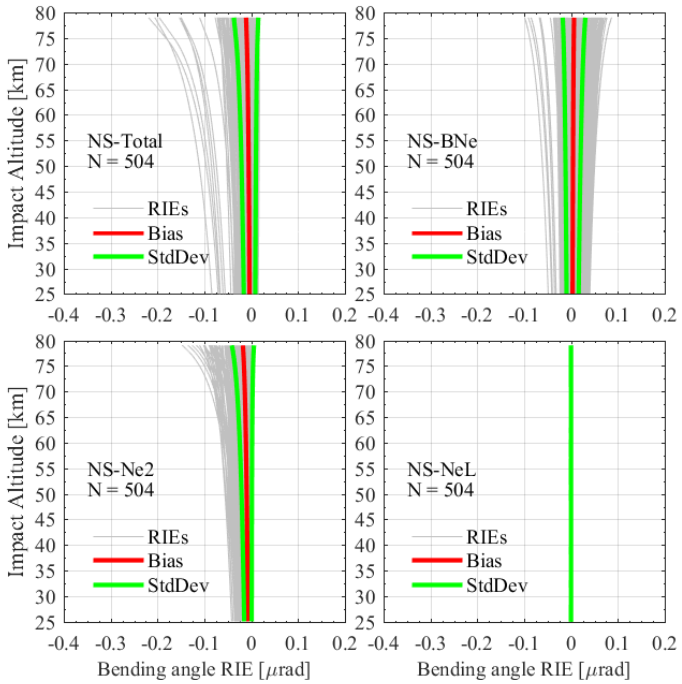

Figure 3.27: *The statistics of the total bi-local bending angle correction and its BNe, Ne2, and NeL components, for the asymmetry ensemble dataset of the Metop-A/-B missions RO events occuring on the three test days*

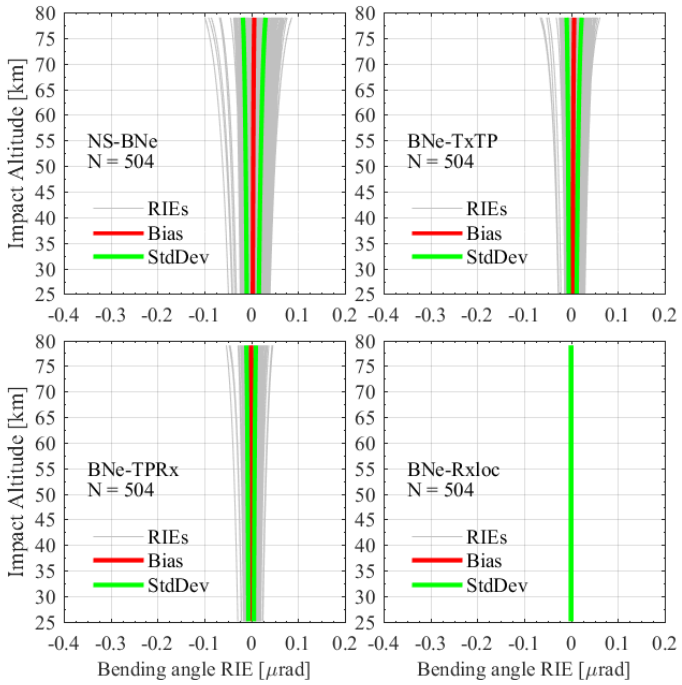

Figure 3.28: *The statistics of the bi-local BNe term and its inbound (TxTP), outbound (TPRx), and Rx location (Rxloc) components, for the asymmetry ensemble dataset of the Metop-A/-B missions RO events occuring on the three test days*

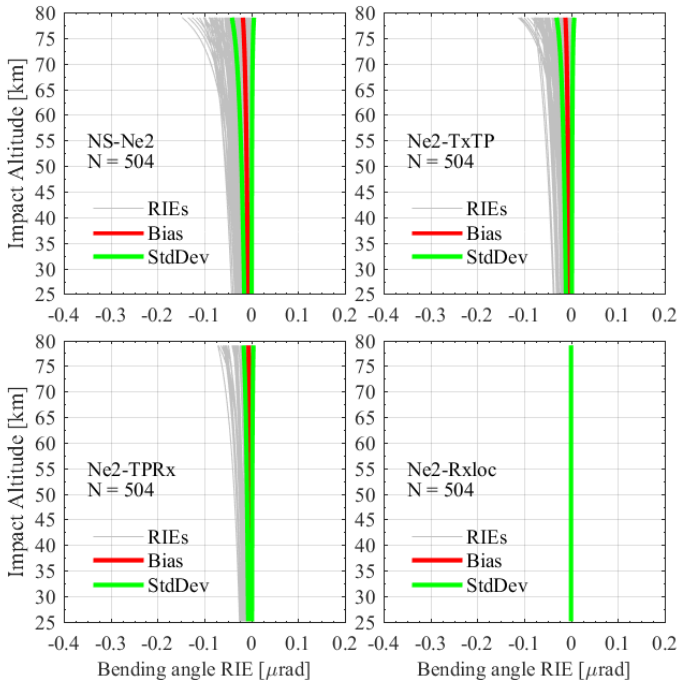

Figure 3.29: *The statistics of the bi-local Ne2 term and its inbound (TxTP), outbound (TPRx), and Rx location (Rxloc) components, for the asymmetry ensemble dataset of the Metop-A/-B missions RO events occuring on the three test days*

3.2.4 Comparison results for different seasonal and regional conditions

In this subsection, we show the comparison results of Bi-local and Kappa correction approaches in different seasonal and regional conditions. For the seasonal and regional comparison, the datasets of Global, Southern Hemisphere High latitude (SHH) and Equatorial Day Time (EDT) zones are used, which are part of the zones summarized in Table 3.1 and which have been used in [RD.12] for previous RIE analyses.

In the Figure 3.30 to Figure 3.34 below, as introduced in the beginning of Chapter 3 for the purpose of direct comparison of Bi-local and Kappa approaches, the fourth subpanel (lower right) of figures shows the Kappa correction term, to appear side-by-side with the Bi-local Ne2 term (lower left). Figure 3.30 to Figure 3.32 show the global results sequentially for each of the three test days, while Figure 3.33 and Figure 3.34 show the regional-zone results for the EDT and SHH regions, respectively.

Please notice that the real bending angle data were used for both bi-local and Kappa approaches, and a vertical moving-average filtering with a ±5 km window width was used over each bending angle profile to suppress vertical small-scale noise.

Table 3.1: *Geographic zone definitions*

Abbreviation	Zone	Latitude range	Longitude (LT) range
GLO	Global	90S-90N	180W-180E
NHH	Northern Hemisphere High-latitude	60N-90N	180W-180E
NHM	Northern Hemisphere Middle-latitude	30N-60N	180W-180E
EDT	Equatorial Day Time	10S-30N	9:00-21:00 LT
SHM	Sorthern Hemisphere Middle-latitude	30S-60S	180W-180E
SHH	Sorthern Hemisphere High-latitude	60S-90S	180W-180E

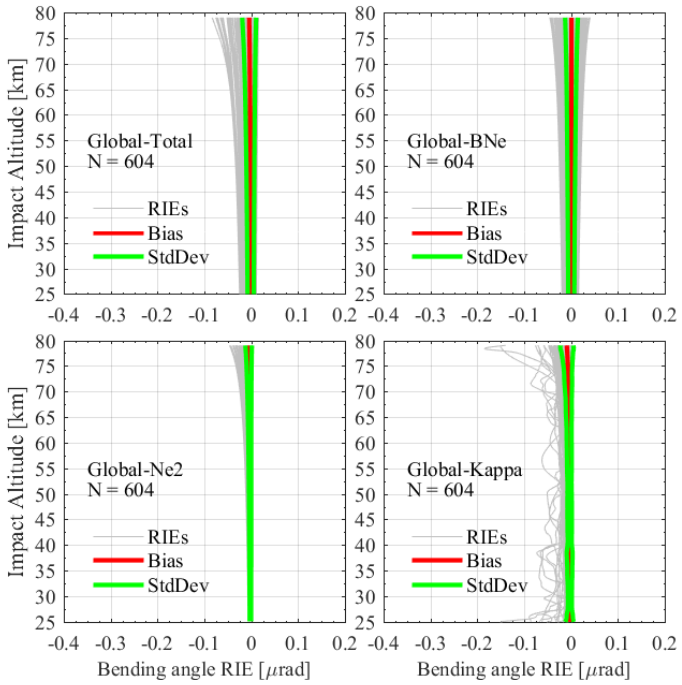

Figure 3.30: *The statistics of the total bi-local bending angle correction and its BNe and Ne2 components, as well as the Kappa bending angle correction, for the global ensemble dataset of the Metop-A mission RO events on July 15th 2008*

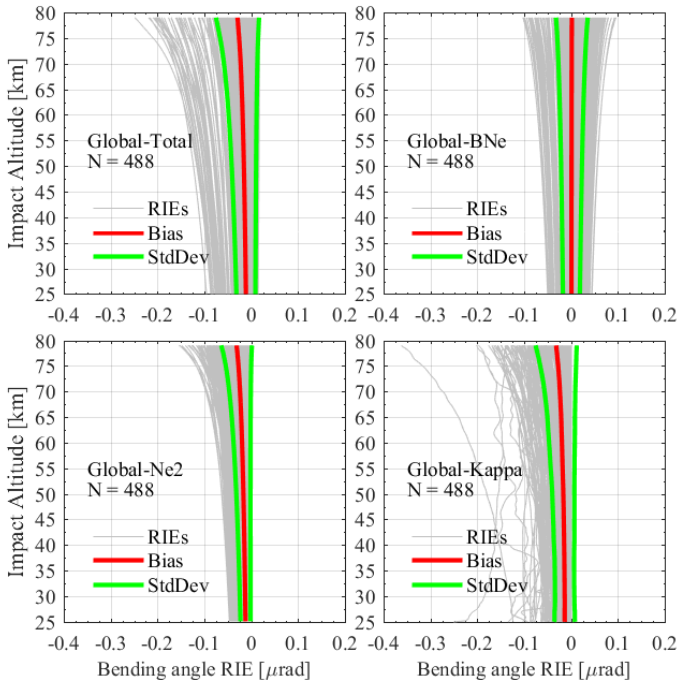

Figure 3.31: *The statistics of the total bi-local bending angle correction and its BNe and Ne2 components, as well as the Kappa bending angle correction, for the global ensemble dataset of the Metop-B mission RO events on May 15th 2013*

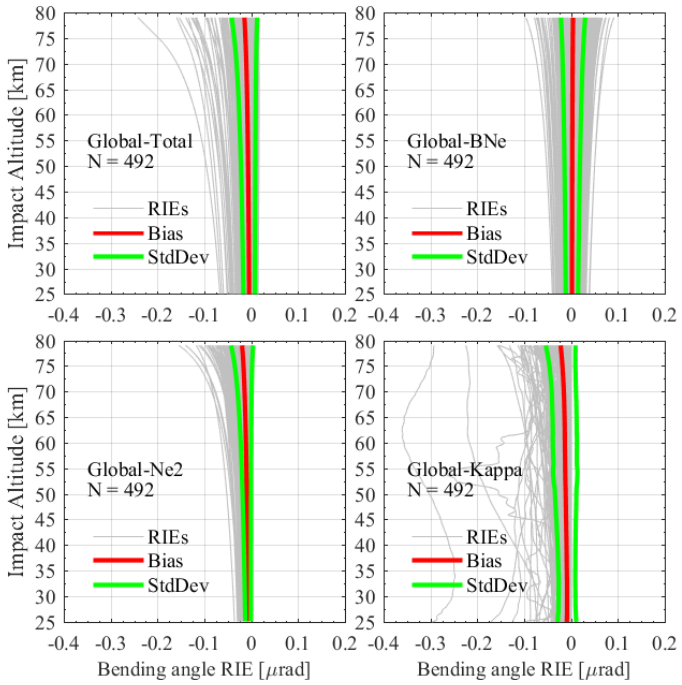

Figure 3.32: *The statistics of the total bi-local bending angle correction and its BNe and Ne2 components, as well as the Kappa bending angle correction, for the global ensemble dataset of the Metop-B mission RO events on July 15th 2013*

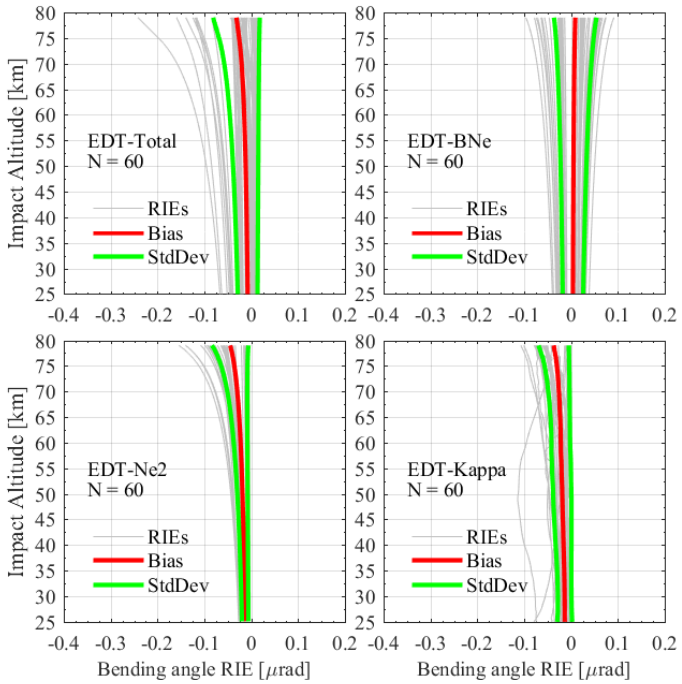

Figure 3.33: *The statistics of the total bi-local bending angle correction and its BNe and Ne2 components, as well as the Kappa bending angle correction, for the EDT ensemble dataset of the Metop-B mission RO events on July 15th 2013*

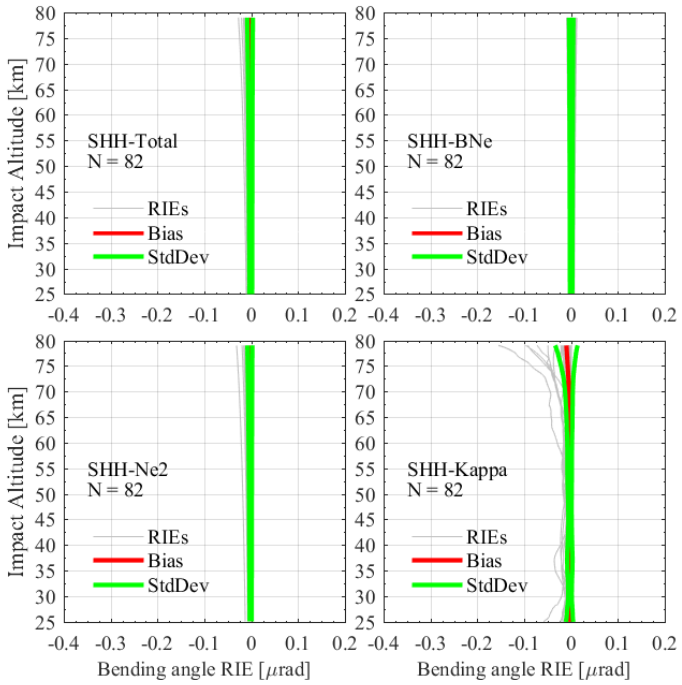

Figure 3.34: *The statistics of the total bi-local bending angle correction and its BNe and Ne2 components, as well as the Kappa bending angle correction, for the SHH ensemble dataset of the Metop-B mission RO events on July 15th 2013*

Comparing the Kappa bending angle RIE with the Ne2 term of the bi-local correction approach, they are similar to each other, which basically validates the (newer) bi-local approach to perform reasonable.
Comparing the regional and seasonal datasets, the bending angle RIEs of the SHH dataset, which represent southern hemisphere high latitude conditions in winter season, are smaller than those of the EDT dataset, which represent equatorial day time zone with significantly higher electron densities than in SHH based on the modeling here.

3.2.5 Direct statistical comparison of the Bi-local approach and Kappa approach

In this subsection, we show direct statistical comparisons of the Bi-local bending angle (total) correction term and the Kappa bending angle correction term. By this we aim to inspect the statistical level of consistency between the two approaches, on the one hand, and to highlight the differences under specific conditions, on the other hand, in particular since the Bi-local correction may capture significantly more variability of conditions with its more sophisticated formulation than the Kappa correction with its more simplified formulation.

To inspect in more detail the histogram of the mean bias in the 75-80 km (upper mesosphere), 50-55 km (near stratopause) and 30-35 km (middle stratosphere) altitude ranges. We use for this purpose the global ensemble dataset of the Metop-A/-B and GRACE mission RO events on the two test days in 2013, where medium to high solar activity conditions provide for useful basic RIE magnitude to better delineate possible differences between detailed statistical characteristics captured by the Bi-local and Kappa approaches.

Figure 3.35 and Figure 3.36 show these results in a histogram format, for the Bi-local total

RIE term (upper left), the Bi-local BNe term (upper right), the Bi-local Ne2 term (lower left), and the Kappa term (lower right). Each of the four panels depicts the histogram in the three representative altitude layers for the middle stratosphere, near stratopause and upper mesosphere.

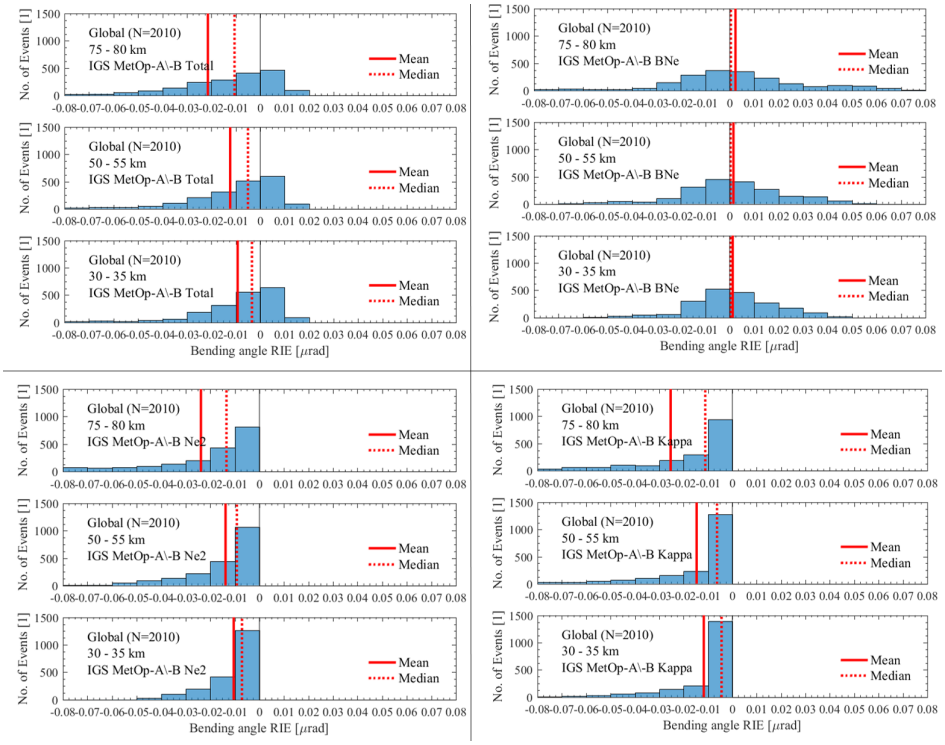

Figure 3.35: *Histogram of bending angle RIE terms in 75-80 km, 50-55 km and 30-35 km altitude ranges (vertical averages in these limited-extent layers), for the IGS case and the Metop-A/-B mission data on the two test days of 2013*

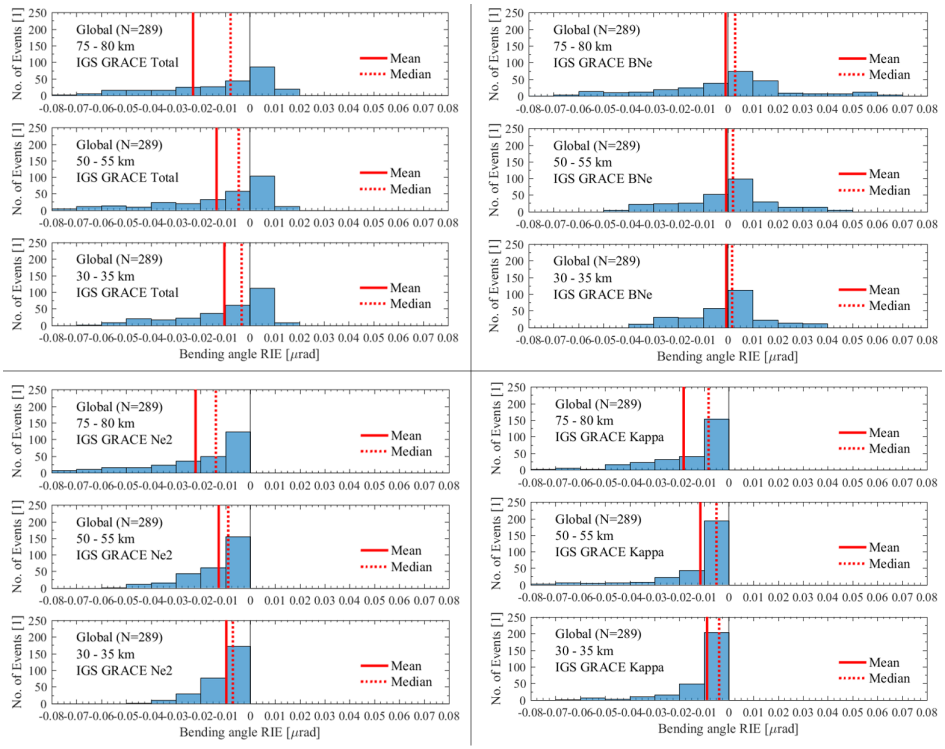

Figure 3.36: *Histogram of bending angle RIE terms in 75-80 km, 50-55 km and 30-35 km altitude ranges (vertical averages in these limited-extent layers), for the IGS case and the GRACE mission data on the two test days of 2013*

From Figure 3.35 and Figure 3.36 we can see that, for the Metop-A/-B missions and GRACE mission, the Bi-local Ne2 term and the Kappa term behave quite similar to each other. The 30-35 km, 50-55 km and 75-80 km layers have a tendency towards exhibiting higher values of the Kappa term (and a somewhat more negative mean), which is a small artefact effect from increased noise in the (real) bending angle difference profiles used in the Kappa term construction.

The mean and median of the Bi-local BNe term appear near zero, while at the same time the BNe term induces a clear variability spreading into the Bi-local total term population, which make its overall characteristics as a histogram population appear significantly broadened against the clear negative-side behavior of the Kappa correction.

3.3 Inter comparison of ionospheric error correction approaches with SABER

3.3.1 Comparison whit SABER data

In this subsection, the comparison analysis of the Standard, Bi-local, and Kappa bending angle correction approaches with independent bending angle profiles derived from SABER pressure and temperature profile observations over the stratosphere and mesosphere is presented.

We have prepared the comparison as a collocation analyses where we maximized the available co-located RO and SABER data for the two test days of 2013, where we can expect

best possible RIE signal under given circumstances due to the medium to high solar activity conditions during these test days. The collocation criteria where selected to be within 300 km and within 3 hours of spatiotemporal distances between the mean locations of the RO and SABER profiles.

Furthermore, a basic quality control (QC) was used for the SABER data, that are partially quite noisy, in which difference profiles of RO and co-located SABER profiles that exceeded 10 μrad anywhere within 45 km to 75 km altitude were discarded from the ensemble. Furthermore, a vertical moving-average filtering with a ±5 km window width was used from 35 km to 75 km altitudes over the difference profiles to suppress vertical small-scale noise that might mask systematic offset-type differences as expected from bulk ionospheric residual terms as modeled by the approaches under study here.

Figure 3.37 shows the collocation ensemble results and one can see that the RO bending angle profiles reasonable align with the independent SABER profiles, although even in the mesosphere above about 60 km a standard deviation near 1 μrad persists, which indicates that with the ensemble size available here a discrimination of potential differences between Bi-local and Kappa approaches at the order of 10^{-8} rad will be challenging.

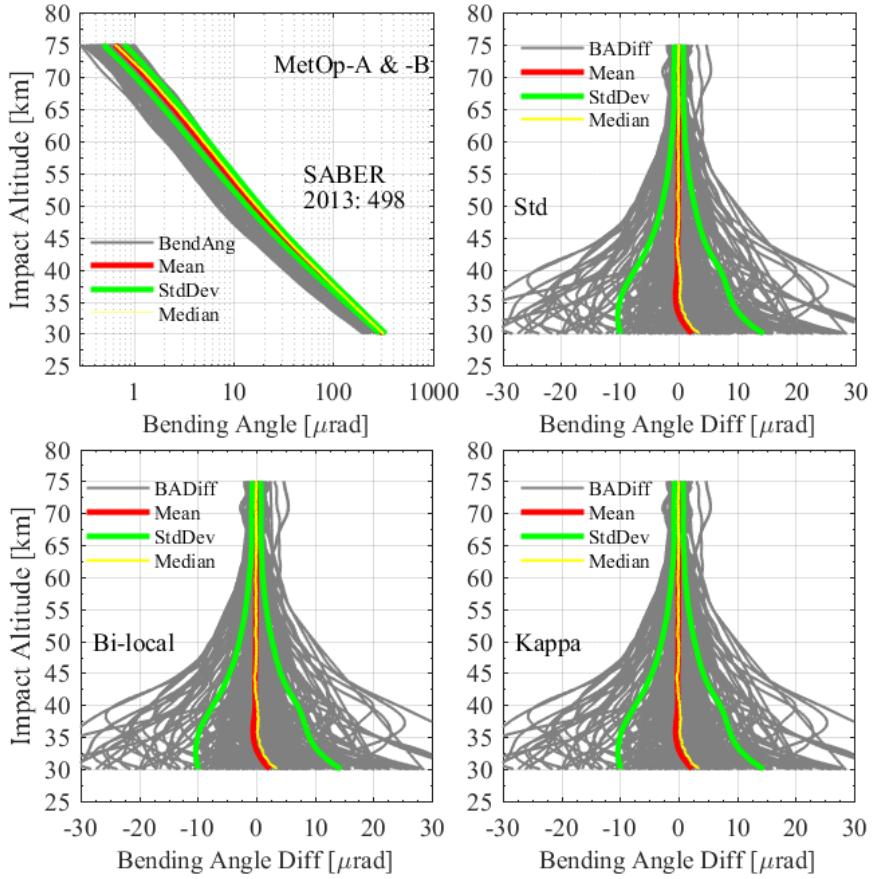

Figure 3.37: *Validation plot of a collocated ensemble of RO bending angle profiles with quality-controlled SABER bending angle profiles, for the Standard (upper right), Bi-local (lower left), and Kappa (lower right) correction approaches, for the two test days in 2013*

3.3.2 Comparison of Bi-local total term and Kappa term

Figure 3.38 and Figure 3.39, this later figure for a collocation ensemble of 2987 profiles pairs, finally show direct comparison profiles of the Bi-local total term and the Kappa term, again as an RIE relative to the standard correction, using the SABER matched collocation ensemble as shown in Figure 3.37 already. This is to inspect with another view whether the SABER data are of sufficient accuracy to descriminate between the two RIE correction methods. The upper-right panels of Figure 3.38 and Figure 3.39 show, though, that the Bi-local and Kappa terms (mean profiles of the ensemble) cannot be discriminated by direct differencing vs. SABER within the double-standard-deviation uncertainty of the mean SABER data (shown as an envelope around the mean RIE term profiles in the upper left panels and amounting to a magnitude of well below 0.01 μrad). While Figure 3.39 uses a much larger dataset with 31 days in July 2013 than that of Figure 3.38 with just two days (15th May and 15th July 2013), and while this is sufficient to show that the Bi-local term is different from the Kappa term given estimated random uncertainties (upper-left), it is clear that also in this case the overall systematic uncertainty of SABER (seen to be of order 0.03 μrad given the deviation of all difference profiles from the "zero line" in the upper-right panel) is too large to practically allow inferences in absolute terms which approach is better.

Also the direct plotting of the terms (lower panels) indicates, that the spread of the profiles is too big for clear descrimination of differences, apart from the fact that a small number of Kappa term reconstructions is hampered by noisy bending angle data (visible as anomalously larger profiles in the lower right panel) and that a small number of Bi-local term reconstructions show spikes from about 40 km downward (which is an artifact from a LEO local term that would be neglected in practical application).

Overall, it is hence clear that a genuine validation of the new correction methods needs a larger collocation ensemble than used for SABER here, with these data from days/times with highest possible ionization levels to maximize the RIE magnitudes, and in particular a somewhat better data quality than available from the present SABER data of which their own systematic uncertainty is larger than the differences between the RIE correction approaches. This may be investigated as part of follow-on studies.

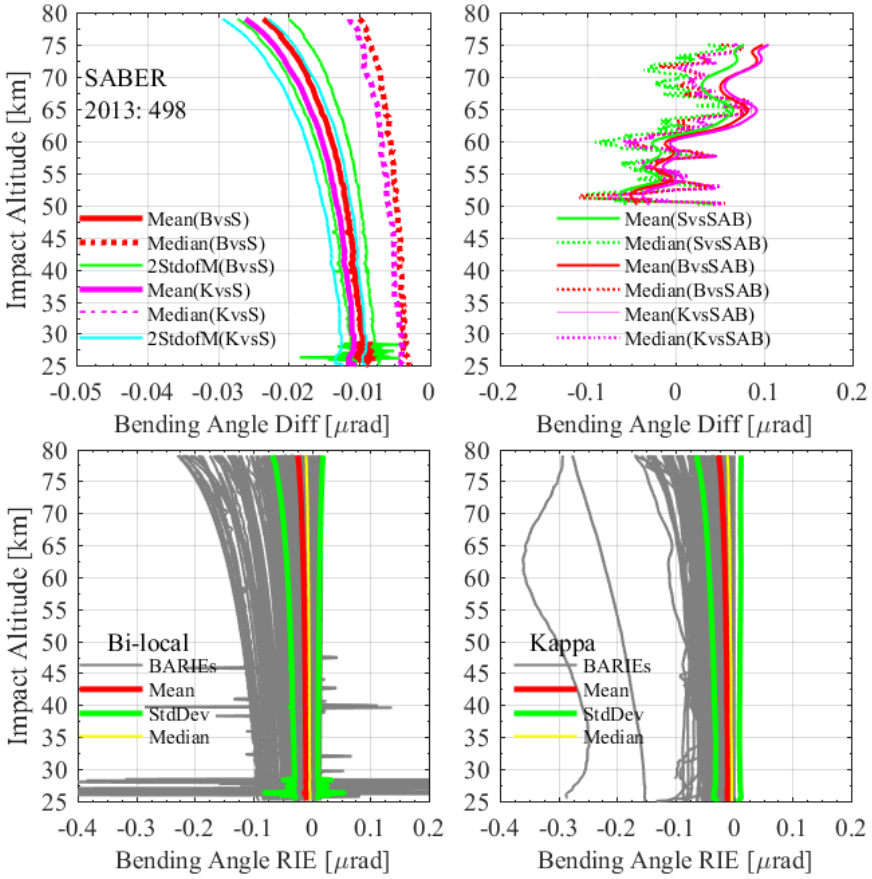

Figure 3.38: *Comparison statistics of Bi-local bending angle correction and Kappa bending angle correction results, using the collocation ensemble of Metop-A/-B missions data with the SABER data on the two test days in 2013, and indicating SABER uncertainty-of-the-mean envelopes about the mean RIE correction terms in the upper left panel*

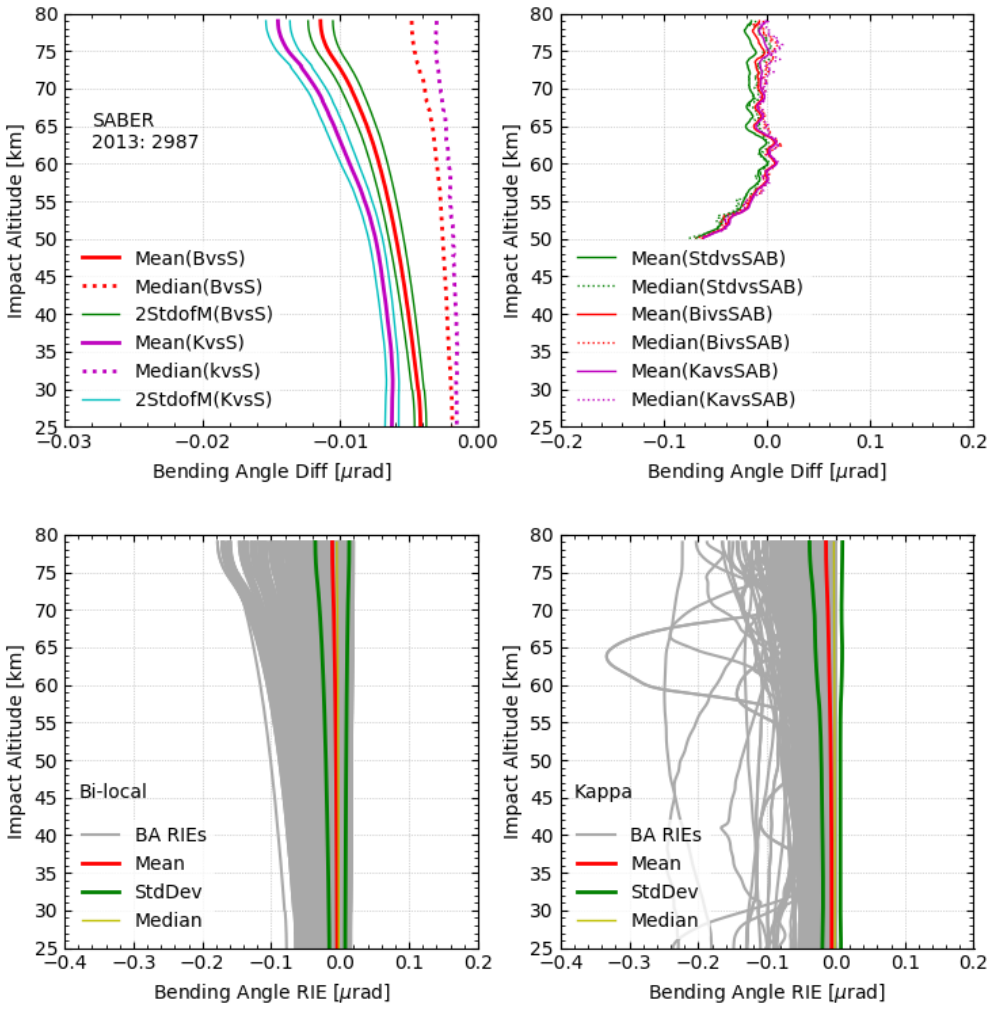

Figure 3.39: *Comparison statistics of Bi-local bending angle correction and Kappa bending angle correction results, using the collocation ensemble of Metop-A mission data with the SABER data on 31 test days in July 2013, and indicating SABER uncertainty-of-the-mean envelopes about the mean RIE correction terms in the upper left panel*

4 Summary, conclusions and recommendations

Based on an implementation of the Bi-local correction approach and the Kappa correction approach in Wegener Center's new rOPS processing system, a first detailed evaluation and statistical comparison analysis has been performed between these two higher-order ionospheric correction approaches for RO bending angle profiles. Additionally, a comparison of these two advanced ionospheric correction approaches with the standard linear dual-frequency bending angle correction method and SABER data has been done. The study showed that the newly introduced Bi-local approach performs reasonable, and in many aspects similar to the more simple Kappa approach, though also important differences have been revealed.

Main overall conclusions that we can draw from the study include the following:

(1) The mean bending angle RIE biases have a clear negative tendency, an aspect where Bi-local and Kappa approaches are closely consistent.

(2) In the three components of the Bi-local term, the Ne2 term plays a dominant role; the geomagnetic term (BNe term) can be important regionally.

(3) The total RIEs clearly increase with increasing solar activity, overall well captured both by Bi-local and Kappa approaches.

(4) The middle latitude bending angle RIEs are larger than the high latitude ones, which is consistent with previous studies.

Following these overall conclusions, we can formulate some recommendations on what we learned more specifically from the performance of the Bi-local correction approach relative to the Kappa correction approach; in order to suggest what might be taken as next steps related to improving ionospheric correction in ROM SAF operational processing, if one considers to go beyond the Kappa approach:

(1) The Bi-local correction approach considers both the effects of the ionospheric electron density and the geomagnetic field, while the Kappa RIE correction approach only considers the effect of the ionosphere; therefore the Bi-local approach has more capacity to present the variability of the Earth space environment conditions that affect RO bending angles.

(2) Although the geomagnetic field term only slightly affects the global-mean climatological bending angle profiles, it may play an important role for the regional-mean climatological bending angle profiles.

(3) The Bi-local correction approach also accounts for the asymmetry of the ionospheric and geomagnetic conditions, which we find to have a moderate but non-negligible influence.

(4) Commonly, the bi-local bending angle RIE corrections are somewhat larger than those of the Kappa approach, while the mean profiles are often reasonable close, moreover, the bi-local approach can capture the smart simplified setup of the Kappa approach.

Further detailed analysis of Bi-local RIE correction approach should investigate the following aspects, among others:

(a) Analyze the bi-local RIE terms using more different missions data (Metop-A/-B, GRACE, COSMIC, FY-3C/-3D GNOS).

(b) Further evaluate the bi-local RIE correction approach comparing with standard method, Kappa approach; larger ensemble SABER validation by using datasets from larger time periods.

(c) Analyze the impact of RIEs, and the corrections, in Level 2 data products (e.g. refractivity, pressure, temperature).

5 Acknowledgments

VS Dr. Congliang Liu expresses many thanks in particular to Prof. Gottfried Kirchengast at WEGC, University of Graz, and Dr. Stig Syndergaard at ROM SAF, DMI Copenhagen, for guiding this visiting scientist study and sharing their great scientific ideas of the GNSS RO bending angle RIE correction approaches; particularly Prof. Kirchengast guided in all aspects of implementing the Bi-local correction approach in the rOPS system and analyzing its performance, and then advised on and coauthored the VS study. Many thanks also to Dr. Kent Lauritsen, ROM SAF, for arranging the management and meetings related to this study and Dr. Sean Healy at ECMWF for joining the meetings and valuable discussions and feedback that also helped improve the report. The half-year ROM SAF Visiting Scientist activity at WEGC was a meaningful and impressed research experience, and VS Dr. Liu also wishes to appreciate all WEGC colleagues for friendly, fruitful, and encouraging discussions, in particular the further coauthors Dr. Marc Schwaerz for all the technical-scientific and programming support and Dr. Julia Danzer for all the scientific discussions and inputs related to the Kappa method.

6 References

[RD.1] Angling, M. J., S. Elvidge, and S. B. Healy, Improved model for correcting the ionospheric impact on bending angle in radio occultation measurements, Atmos. Meas. Tech., 11, 2213-2224, doi:105194/amt-11-2213-2018, 2018.

[RD.2] Zeng, Z., and S. Sokolovskiy, Effect of sporadic E clouds on GPS radio occultation signals, Geophys. Res. Lett., 37, L18817, doi:101029/2010GL044561, 2010.

[RD.3] Zeng, Z., S. Sokolovskiy, W. Schreiner, D. Hunt, J. Lin., and Y-H. Kuo, Ionospheric correction of GPS radio occultation data in the troposphere, Atmos. Meas. Tech., 9, 335-346, doi:10.5194/amt-9-335-2016, 2016.

[RD.4] Syndergaard S., On the ionospheric calibration in GPS radio occultation measurements, Radio Sci., 35, 865-883, 2000.

[RD.5] Vorob'ev, V. V., and G. K. Krasil'ikova, Estimation of the accuracy of the atmospheric refractive index recovery from Doppler shift measurements

[RD.6] Healy, S. B., and I. D. Culverwell, A modification to the standard ionospheric correction method used in GPS radio occultation, Atmos. Meas. Tech., 8, 3385-3393, doi:105194/amt-8-3385-2015, 2015.

[RD.7] Danzer, J., S. B. Healy, and I. D. Culverwell, A simulation study with a new residual ionospheric error model for GPS radio occultation climatologies, Atmos. Meas. Tech., 8, 3395-3404, doi:105194/amt-8-3395-2015, 2015.

[RD.8] Qu, X., Z. Li, J. An, and W. Ding, Characteristics of second-order residual ionospheric error in GNSS radio occultation and its impact on inversion of neutral atmospheric parameter, J. Atmos. Solar-Terr. Phys., 130-131, 159-171, 2015.

[RD.9] Liu, C. L. et al., Characterization of residual ionospheric errors in bending angles using GNSS RO end-to-end simulations, Adv. Space. Res., 52, 821-836, 2013.

[RD.10] IROWG-5 Minutes: Full Minutes, Summary of the workshop, http://irowg.org/;http://irowg.org/wpcms/wp-content/uploads/2017/05

[RD.11] Syndergaard, S., and G. Kirchengast, Theory on ionospheric residual errors in radio occultations (in preparation), November 2019.

[RD.12] Liu, C. L. et al., Quantifying residual ionospheric errors in GNSS radio occultation bending angles based on ensembles of profiles from end-to-end simulations, Atmos. Meas. Tech., 8, 2999-3019, doi:10.5194/amt-8-2999-2015, 2015.

[RD.13] Danzer, J., B. Scherllin-Pirscher, and U. Foelsche, Systematic residual ionospheric errors in radio occultation data and a potential way to minimize them, Atmos. Meas. Tech., 6, 2169-2179, doi:10.5194/amt-6-2169-2013, 2013.

[RD.14] Syndergaard, S. and G. Kirchengast, A bi-local estimation approach for residual ionospheric correction of radio occultation bending angles, poster at EUMETSAT ROM SAF-IROWG International Workshop 19-25 September 2019 (http://www.romsaf.org/romsaf-irowg-2019), Konventum/Elsinore, Denmark, 2019.

[RD.15] Feltens, J. The international GPS service (IGS) ionosphere working group. Adv Space Res 2003, 31, 635-644.

[RD.16] Theault, E., C. C. Finlay, C. D. Beggan, et al., International geomagnetic reference field: The 12th generation. Earth, Planets and Space 2015, 67.

[RD.17]Kirchengast, G., M. Schwarz, J. Schwarz, et al., The reference occultation processing system approach to interpret GNSS radio occultation as SI-traceable planetary system refractometer, presentation at OPAC-IROWG International Workshop 8-14 September 2016 (http://wegcwww.uni-graz.at/opacirowg2016), Seggau/Leibnitz, Austria, 2016.

[RD.18]Kirchengast, G., M. Schwarz, B. Angerer, et al., Reference OPS DAD-Reference Occultation Processing System (rOPS) Detailed Algorithm Description, Tech. Rep. for ESA and FFG No.1/2018, Doc-Id: WEGC-rOPS-2018-TR01, Issue 2.0, Wegener Center, University of Graz, Graz, Austria, 2018.

7 Acronyms and Abbreviations

BG	Background
BDS	BeiDou navigation Satellite system
CHAMP	Challenging Mini–Satellite Payload
CLIMAP	Climate and Environment Monitoring with GPS–based Atmospheric Profiling (EU)
CODE	Centre for Orbit Determination in Europe
COSMIC	Constellation Observing System for Meteorology, Ionosphere & Climate
DMI	Danish Meteorological Institute
ECF	Earth–centred, Fixed coordinate system
ECI	Earth–centred, Inertial coordinate system
ECMWF	The European Centre for Medium-Range Weather Forecasts
EOP	Earth Orientation Parameters
ESA	European Space Agency
EU	European Union
EUMETSAT	European Organisation for the Exploitation of Meteorological Satellites
GALILEO	European GNSS constellation project (EU)
GLONASS	Global Navigation Satellite System (Russia)
GNSS	Global Navigation Satellite Systems (generic name for GPS, GLONASS, GALILEO and BDS)
GPS	Global Positioning System (US)
GPS/MET	GPS Meteorology experiment, onboard Microlab-1 (US)
GRAS SAF	Consortium formed to define and prepare the Operational GRAS SAF. Members are DMI (leader), UKMO and IEEC.
GRACE	GRAvity Recovery and Climate Experiment
GTS	Global Telecommunications System
IGS	International GPS Service
LEO	Low Earth Orbited
LOS	Line Of Sight
METOP	Meteorological Operational polar satellites (EUMETSAT)
NRT	Near Real Time
NWP	Numerical Weather Prediction
POD	Precise Orbit Determination
Q/C	Quality Control
RIE	Residual Ionospheric error
RO	Radio Occultation
ROM SAF	The EUMETSAT Satellite Application Facility responsible for operational processing of radio occultation data from the Metop satellites. Members are DMI (leader), UKMO, ECMWF and IEEC.
ROPP	Radio Occultation Processing Package
SAC–C	Satelite de Applicaciones Cientificas – C
SAF	Satellite Application Facility (EUMETSAT)
SI	Système International (The MKS units system)
TP	Tangent Point
UT1	Universal Time-1 (proportional to the rotation angle of the Earth)
UTC	Universal Time Coordinated
WGS–84	World Geodetic System, 1984. (US DoD)

WMO World Meteorological Organization